UNIVERSITÀ DEGLI STUDI DI PADOVA

Dipartimento di Fisica e Astronomia "Galileo Galilei"

Master Degree in Physics of Data

Final Dissertation

Dynamical Mean Field Theory and Applications to Ecological and Neural Systems

Thesis Supervisor

Prof. Samir Simon Suweis

Thesis Co-supervisor

Prof. Amos Maritan

Candidate

Marco Zenari

Student ID

2097012

Academic Year 2023/2024

Acknowledgements

Abstract

In this Master thesis, we explore the intricate applications of Dynamical Mean Field Theory (DMFT) in unraveling the complexities of ecological and neural systems. The study begins with an in-depth analysis of the DMFT framework, introducing the procedure for its derivation, and emphasizing its utility in simplifying complex interacting systems into a set of effective self-consistent equations with reduced dimensionality. This theoretical groundwork is pivotal for understanding the subsequent applications of the theory.

The thesis then progresses to the application of DMFT to ecological systems, with a specific focus on the Generalized Lotka-Volterra (GLV) systems characterized by quenched disorder. A significant aspect of this exploration is the examination of how the saturation of interactions between species influences the dynamics of these systems. This inquiry, carried out with linear response theory, explores the various response mechanisms within GLV systems and their effect on system behavior and stability. With DMFT it is also possible to compute self-consistently the species abundance distribution in the stable phase of the system.

Extending the scope of DMFT, the thesis also investigates its application in the field of neuroscience, particularly within recurrent neural networks. This segment of the study focuses on identifying the conditions that lead to the emergence of a reservoir of multiple timescales, akin to the behaviors observed in cortical neural circuits. This exploration provides valuable insights into the mechanisms that underlie neural processing and information storage.

Finally, the thesis incorporates an empirical analysis of neural datasets to correlate theoretical findings with real-world data. This crucial part of the work aims to highlight the emergence of a reservoir of timescales in cortical circuits, grounding the theoretical work on recurrent neural networks, and serves as a critical evaluation of the DMFT framework. By juxtaposing theoretical predictions with actual data, the thesis aims to validate the effectiveness of DMFT in practical applications and highlights areas that might require further development or refinement.

Overall, this Master thesis offers a significant contribution to the fields of theoretical physics, ecology, and neuroscience, presenting new perspectives and methodologies for understanding the dynamics of complex systems in an interconnected world.

Contents

Chapter 1

Introduction

The recent increase of interest in complex systems has led to a rich and interdisciplinary research field that spaces among a large variety of disciplines, characterized by completely different mechanisms and scales. Although there is a general scientific consensus on what is meant by complexity, a formal and satisfactory definition of complex systems still misses and goes beyond the aim of this brief introduction. Here we limit ourselves to present what is meant by complex systems in the physics community, according to the seminal works of Anderson [1], Goldenfeld and Kadanoff [2], and then summarized by Newman in a review [3]. In nature, systems made up of a large number of units that interact and connect with each other in a non-trivial way are ubiquitous. Their interactions give rise to emergent collective phenomena, such as self-organization in biological systems [4]. Even when the single agent dynamics is very well understood, the collective behavior of the system is often difficult to explain. This concept, summarized with the aphorism *more is different* [1], suggests that when individual components interact, their collective dynamics can exhibit emergent properties that are not apparent from the behavior of the individual components alone. These emergent properties can lead to complex, often unpredictable, macroscopic phenomena that cannot be straightforwardly inferred by simply analyzing the system's parts in isolation. And in these cases, effective emergent description of the systems are thus necessary. For example, the computational effort to predict the dynamics of a system composed by milions of particles from its fundamental (Netwon's) laws is unfeasible. Apart from the computation, the problem is actually conceptual. Even with infinite computational resources, the fundamental laws could only be used to simulate the complete system and observe its microscopic behavior, without getting any actual comprehension of what are the relevant control parameters driving the observed emergent macroscopic behavior.

A possible different approach when dealing with a complex system is, from a theoretical point of view, to develop models that comprehend few essential minimal features of the system and are able to reproduce its emergent patterns. Since a general theory for complex systems is far from being achieved, there is no standard procedure to obtain such a model, but each particular system has to be considered separately. Moreover, preferably these minimal models should be simple enough to be approachable with effective analytical tools. In particular, some interesting analytical results can be obtained by exploiting statistical physics methods in the limit of infinite units (e.g., the thermodynamic limit). These tools are borrowed and adjusted for complex systems from the fields of stochastic processes [5, 6], non-equilibrium statistical physics [7, 8], complex networks [9], and theory of disordered systems [10]. A famous example is the replica method developed by Parisi [11] for the study of spin glasses that is now applied consistently in ecology. Recently, methods based on path integrals [12] and generating functional analysis [13] have given interesting results in capturing the dynamic of systems, thanks to the theoretical framework developed within Dynamical Mean Field Theory (DMFT) [14, 15, 16].

Many complex interacting systems, for example in ecology and neuroscience, can be modeled with a system of coupled differential equations, where each equation models the dynamic of a unit and how it interacts with the others. These systems of equations are usually difficult to solve, even in the stationary regime, when the number of degrees of freedom is large. The DMFT offers a procedure

to reduce the dimensionality of such systems by introducing self-consistent effective equations that are equivalent, in the thermodynamic limit, to the initial set of couple differential equations. In the effective equations, a noise term that follows from averaging over quenched disorder appears and captures the variability of the units dynamics. The correlation of the noise has to be determined self-consistently together with the other functions that are introduced in the DMFT equation. The resulting effective equations have to be treated carefully, due to self-consistency, but give an analytical framework in which it is possible to obtain insights and predictions on the macroscopic patterns of the system.

In this thesis, we start with a brief review of the theoretical background of DMFT in Chapter 2, based on the Martin-Siggia-Rose-De Dominic-Janssen formalism [14, 15, 16]. We give a schematic procedure for the derivation of the DMFT of a dynamical system of differential equations with quenched disorder. The details of the derivation for particular systems are discussed in Sect. 3.2 for the Generalized Lotka-Volterra models and in Sect. 4.2 for Recurrent Rate Networks with assemblies. In Chapter 2 we also present an iterative procedure to solve a DMFT equation with observables that must be obtained self-consistently [17]. An application of this procedure is presented in Sect. 3.3 for the Generalized Lotka-Volterra models and is validated with numerical simulations of ordinary differential equations. The thesis then continues exploring the applications of DMFT in ecological and neural systems.

In the field of ecology, different prototypical models have been developed, such as the logistic growth model [18], the MacArthur Consumer Resource model [19] and the Lotka-Volterra model [20]. In recent years, a generalization of the predator-prey Lotka-Volterra model to a larger number of species and different types of interactions has become the standard approach in ecology [21]. In particular, the coefficients that describe the types of interaction (as will be discussed in Sect. 3.1) can be randomly sampled from a given distribution to reduce the number of parameters of the system [22], as in disordered systems. By adding the disorder in the model, the typical tools of disordered systems can be applied, like random matrix theory [23] and the over-mentioned DMFT, leading to the possibility of investigating the stability of the system. The phase diagram of the GLV systems obtained with DMFT [24] is the same as the one obtained with standard methods in Ref. [25]. In this thesis, we modify the standard GLV model with the introduction of a saturation function for the interaction between species with the aim of removing the unfeasible unbounded growth phase that appears in the standard GLV [25]. Another approach with the same aim can be found in Ref. [26], where a non-linear feedback is similarly introduced. Recently, a DMFT for GLV with a specific connectivity matrix has also been developed [27] leading to promising results.

Finally, we investigate the application of DMFT in neuroscience. In this field, Recurrent Neural Networks (RNN) are a versatile tool [28] used to model neural circuitry by constraining the structure of the network according to biological principles [29] or connectome studies [30]. In particular, the study of fluctuations and correlations in RNN has become a relevant open problem in theoretical neuroscience, following the seminal work of Ginzburg and Sompolinsky [31]. Here, we focus on the study of the autocorrelation times of units in neural circuits. Experimental findings show that the empirical distributions of autocorrelation times in cortical circuits are skewed and fat-tailed [32], similarly to lognormal distributions. This emergence of a reservoir of timescales seems to play a fundamental role in the ability of neural circuits to compute complex tasks [33], although the mechanisms at the base of this emergent pattern are yet unknown. In Chapter 5, an empirical analysis of calcium imaging of mouse olfactory bulbs highlights an example of the skewed and fat-tailed distributions of the autocorrelation times mentioned above. The mechanisms for their emergence are investigated in Chapter 4, introducing rate network models with neural assemblies and discussing criticality and heterogeneity of assemblies self-interaction. Different choices for this self-interaction can be made, such as zero or negligible [34] or constant finite value for every unit [35]. The recent work by Ref. [36] suggest the possibility of introducing heterogeneous self-interactions as a possible mechanism for the emergence of the reservoir of timescales. This hypothesis is also supported by the empirical distributions of the sizes of functional ensembles [37].

Chapter 2

Dynamical Mean Field Theory

The *Dynamical Mean Field Theory* (DMFT) is a mathematical formalism based on functionals and path integrals that is often applied in systems with quenched disorder. In the 1970s different authors independently developed the path integral theory, which is the basis for the derivation of DMFT [15, 14, 16]. This path-integral theory is often referred to as the *Martin-Siggia-Rose-De Dominicis-Janssen* path-integral method. The importance of DMFT lies in the possibility of simplifying quenched disordered systems of differential equations into effective self-consistent stochastic differential equations (SDE) that can be used as a starting point to obtain analytical results on the emergent behaviors of the studied system. For this reason, it has been recently employed in the study of many different complex systems, as will be extensively discussed in the following of this thesis. This chapter includes the introduction of elements of functional analysis and stochastic differential equations, which are fundamental mathematical tools in this formalism. A general derivation of the *Martin-Siggia-Rose-De Dominicis-Janssen* path-integral method is presented following recent reviews on the topic [38, 39] and a discussion of the derivation of DMFT is also presented. The formalism and notation introduced in this section will be adopted and adapted for different systems in the following chapters, where the precise DMFT for each particular model will be derived. Finally, a numerical implementation of DMFT developed by Ref. [17] is proposed.

2.1   Elements of Functional Calculus

In this section the basic definitions and rules of functional analysis are presented for the sake of completeness. For extensive studies on the subject, we refer you to specialized texts.

Definition: Functional
A functional is a map from the space of smooth functions $\mathcal{C}$ to the space of real numbers $\mathbb{R}$:

$$f : \mathcal{C} \mapsto \mathbb{R}. \tag{2.1}$$

Definition: Functional Derivative
The derivative of a functional in a point x is defined as

$$\frac{\delta f[x]}{\delta x(t)} := \lim_{\epsilon \to 0} \frac{f[x + \epsilon\phi] - f[x]}{\epsilon}, \tag{2.2}$$

if the limit exists for every smooth function $\phi(t)$ and it measures the sensitivity of the dependence of the functional on the argument in the point $x(t)$. From the definition follows the linearity of the derivative and the fact that the derivative is done with respect to a particular time. Eq. (2.2) can be mapped

to the usual definition of derivative for real functions, introducing the function $F(\epsilon) := f[x + \epsilon\phi]$, and obtaining

$$\frac{\delta f[x]}{\delta x(t)} = \frac{d}{d\epsilon}F(\epsilon)|_{\epsilon=0}. \tag{2.3}$$

The usual derivation rules follow from this connection with traditional mathematical analysis.

Product Rule
Exploiting Eq. (2.3) is easy to show that:

$$\frac{\delta}{\delta x(t)}(f[x]g[x]) = \frac{\delta f[x]}{\partial x(t)}g[x] + f[x]\frac{\delta g[x]}{\partial x(t)}. \tag{2.4}$$

Chain Rule
Consider a map $g : \mathcal{C} \mapsto \mathcal{C}$ and its composition with a functional $f[g[x]]$. By discretizing the t-axis with N steps, applying the chain rule in $\mathbb{R}^N$ and taking the limit of infinitesimal discretization it is possible to show the chain rule:

$$\frac{\delta}{\delta x(t)}f[g[x]] = \int ds \frac{\delta f[g]}{\delta g[x](s)} \frac{\delta g[x](s)}{\delta x(t)}. \tag{2.5}$$

Functional of Fourier Transform
If the case in which we consider a function $x(t)$ and its Fourier transform $\tilde{X}(\omega)$, that is, $x(t) = \frac{1}{2\pi}\int e^{i\omega t}\tilde{X}(\omega)d\omega$, as arguments of two functionals f and $\hat{f}$ such that $\hat{f}[\tilde{X}] = f[x]$, it is possible to use the chain rule (2.5), obtaining

$$\frac{\delta\hat{f}[\tilde{X}]}{\delta\tilde{X}(\omega)} = \frac{\delta}{\delta\tilde{X}(\omega)}f\left[\frac{1}{2\pi}\int e^{i\omega t}\tilde{X}(\omega)d\omega\right] = \int ds \frac{\delta f[x]}{\delta x[s]}\frac{\delta x(s)}{\delta X(\omega)} = \int ds \frac{\delta f[x]}{\delta x[s]}\frac{e^{i\omega s}}{2\pi}. \tag{2.6}$$

This relationship is helpful to evaluate expressions of the following form

$$\int \frac{\delta f[x]}{\delta x(s)}y(s)ds = \int \frac{1}{2\pi}\int \frac{\delta f[x]}{\delta x(s)}e^{i\omega s}\tilde{Y}(\omega)d\omega ds = \int \frac{\delta\hat{f}[\tilde{X}]}{\delta\tilde{X}(\omega}\tilde{Y}(\omega)d\omega, \tag{2.7}$$

which are therefore invariant under Fourier transform.

Functional Taylor series
Another useful result is the generalization of a Taylor series for a functional f of a field $x(t)$, which is used, for example, in Linear Response Theory (at first order) or in perturbative methods [38]. Applying the functional derivative definition and the product rule one obtains the following expansion around $x(t) \simeq 0$

$$f[x] = \sum_{n=0}^{\infty}\int dt_1...\int dt_n \frac{1}{n!}\frac{\delta^n f}{\delta x(t_1)...\delta x(t_n)}\prod_{i=1}^{n}x(t_i), \tag{2.8}$$

which can be easily generalized to a point x_0 by replacing $x \to x - x_0$.

2.2 Elements of Stochastic Differential Equations

In the field of complex systems, the dynamic is often described with differential equations in which the presence of fluctuations (the causes of which can be many) is represented by stochastic terms.

The resulting equations are named *Stochastic Differential Equations* (SDE) and are often written in the following form:

$$dx(t) = f(x)dt + g(x)dW(t) \tag{2.9}$$

where dW is the stochastic increment and $f(x)$ is the deterministic part. They are usually solved starting from an initial condition $x(0^+) = a$. Their formal definition relies on the discretization of time in a lattice of spacing h and on the existence of the limit $h \to 0$. For the discretization, different conventions are possible, depending on the point where the functions are computed when studying the trajectories. In general, the discretization of Eq. (2.9) can be written as

$$x_i - x_{i-1} = f\left(\alpha x_i + (1-\alpha)x_{i-1}\right)h + g\left(\alpha x_i + (1-\alpha)x_{i-1}\right)\xi_i + a\delta_{i,1}, \tag{2.10}$$

where h is the discretization time step, $\alpha \in [0,1]$, the term $a\delta_{i,1}$ is the initial condition and ξ_i is a stochastic increment such that $\xi = \frac{dW}{dt}dt$ and it is often chosen from a normal distribution according to the Wiener process [40]. The two most used conventions are the Ito $\alpha = 0$ and the Stratonovich $\alpha = 1/2$ [41] that yield the same continuous time limit in the case of additive noise $g(x) = const$, but the drift term lead to different path integral representations depending on the chosen convention.

Assuming that the noise is sampled independently at each time step as in white noise, the probability density of the points $x_1, ..., x_M$ along the path $x(t)$ can be written as

$$p(x_1, ..., x_M) = \int \prod_{i=i}^{M} d\xi_i \rho(\xi_i) \delta(x_i - y_i(\xi_i, x_{i-1})), \tag{2.11}$$

where we indicate with $\rho(\xi)$ the probability distribution from which ξ is sampled at every iteration and with $y_i(\xi_i, x_{i-1})$ the solution Eq. (2.10) which depends on the choice of α. For example, in the Ito convention ($\alpha = 0$) we have $y_i(\xi_i, x_{i-1}) = x_{i-1} + f(x_{i-1})h + a\delta_{i,1} + \xi_i$, while in the Stratonovich convention ($\alpha = 1/2$) there is no explicit form for y_i since the argument of f and g depends on x_i. Note also that in Eq. (2.11) the assumption that y_i depends only on x_i implies that the solution x_i depends only on the solution x_{i-1} in the previous step, and not on $x_{i-2}, x_{i-3}, ...$ Processes with this property are called *Markov processes*.

2.3   Martin-Siggia-Rose-De Dominicis-Janssen Path Integral

In standard path integral approaches, like the one by Onsager and Machlup [42, 43], the idea is to start from Eq. (2.11) and substitute the expression for $y(\xi_i, x_{i-1})$ obtained by solving Eq. (2.10) which can easily be done, for example, in the Ito convention. Assuming Gaussian noise $\rho(\xi_i) = \mathcal{N}(0, Dh)$ with zero mean and variance that depends linearly on the integration step h with coefficient D, if the continuum limit $h \to 0$ can be computed, it is possible to obtain an integral measure for the process [42, 43] and the corresponding probability density. The disadvantage of this approach is that the resulting probability density depends on a quadratic term that complicates the computation of quenched averages in disordered systems [38].

The idea of the MSRDJ approach is to introduce an auxiliary field $\tilde{x}$ that enters the probability definition (2.11) and has the appreciated characteristic of simplifying the computation of quenched averages and response functions. The procedure consists in representing the Dirac-Delta distribution with its Fourier integral

$$\delta(x) = \frac{1}{2\pi} \int_{-\infty}^{+\infty} d\tilde{x} e^{i\tilde{x}x} \tag{2.12}$$

in Eq. (2.11), obtaining the form:

$$p(x_1, ..., x_M) = \prod_{i=1}^{M} \left[\int d\xi_i \rho(\xi_i) \frac{1}{2\pi} \int_{-\infty}^{+\infty} d\tilde{x}_i e^{i\tilde{x}_i(x_i - x_{i-1} - y_i(\xi_i, x_{i-1}))} \right]. \tag{2.13}$$

Note that in Eq. (2.13) the argument of the exponential contains information on the dynamics of the system $x_i - x_{i-1} - y_i(\xi_{i-1}, x_i)$. In particular, the information on the stochastic process and the convention chosen is contained in the form of $y_i(\xi_{i-1}, x_i)$.

It is also useful to introduce the moment-generating functional, obtained by adding the terms $\sum_{l=1}^{M} \psi_l x_l h$ to the action in Eq. (2.13) and integrating over all paths:

$$Z(\psi_1, ..., \psi_M) := \prod_{l=i}^{M} \left[\int_{-\infty}^{+\infty} dx_l \exp\left(\psi_l x_l i h\right) \right] p(x_1, ..., x_M). \tag{2.14}$$

Introducing the notation $\prod_{l=1}^{M} \int_{-\infty}^{+\infty} dx_l \rightarrow \int \mathcal{D}x$ and $\prod_{l=1}^{M} \int_{-\infty}^{+\infty} d\tilde{x}_l/(2\pi) \rightarrow \int \mathcal{D}\tilde{x}$ in the continuum limit $h \rightarrow 0$ we denote the path integral as the generating functional

$$Z(\psi) = \int \mathcal{D}x \mathcal{D}\tilde{x} \exp\left(i \int dt \psi(t) x(t)\right) \exp\left(i \int dt (\dot{x}(t) - f(x(t), t)) \tilde{x}(t))\right), \tag{2.15}$$

where $\psi(t)$ is the source field and $f(x(t), t)$ contains the dynamics of x according to $\dot{x}(t) = f(x(t), t)$.

It is easy to show that computing the derivative of the Moment Generating functional with respect to the source field ψ yields moments of the distribution of $x(t)$ at time t. For example one can compute the average of x at time t

$$\frac{\partial}{\partial \psi(t)} Z(\psi)|_{\psi=0} = \int \mathcal{D}x \mathcal{D}\tilde{x} x(t) \exp\left(i \int dt (\dot{x}(t) - f(x(t), t)) \tilde{x}(t))\right) = \langle x(t) \rangle, \tag{2.16}$$

or n-th order moments performing an n-th order functional derivative

$$\langle x(t)...x(s) \rangle = \frac{\delta^n}{\delta \psi(t)...\delta \psi(s)} Z[\psi]|_{\psi=0}. \tag{2.17}$$

2.4 Dynamical Mean Field Theory

Systems with many interacting degrees of freedom are ubiquitous in the field of complexity science. These systems have interesting properties both at equilibrium and out-of-equilibrium, therefore a description of their dynamics is needed. For this reason, they are often modeled with systems of coupled differential equations that depend on some parameters. Typically, the number of parameters of the model is very large, leading to very complicated equations that cannot be solved analytically. An interesting approach, derived from the field of disordered systems, consists of assuming that the parameters of the model are sampled from a given probability distribution. In this thesis quenched disorder is considered, and therefore the value of the parameters is sampled once at the beginning and kept the same for the evolution of the system. In these circumstances, a common approach is to develop a mean-field theory of the system that introduces effective equations for the system. The Dynamical Mean Field Theory gives the possibility to obtain such effective equations that represent the dynamics of the system. These equations can be performed in a formal and robust way for disordered systems starting from the definition of a moment-generating functional (2.15) and evaluating it in the thermodynamic limit. The procedure for obtaining the DMFT is common and is presented in this section, but the details of the calculations depend on the details of the system.

The DMFT derivation starts from a system of coupled differential equations that describe a complex system. Historically, these equations are deterministic (once the disorder is quenched), but generalizations to stochastic differential equations have been made [38, 44]. In what follows, we start with ordinary differential equations (ODE)

$$\dot{x}_i = F_i(t, x_1, ..., x_N | \theta) \qquad i = 1, ..., N, \tag{2.18}$$

where with θ we indicate the set of parameters of the model, distributed accordingly to a probability distribution $P(\theta)$. For this dynamics, we can define a moment-generating functional as defined by Eq. (2.15)

$$Z[\psi] = \int \mathcal{D}\mathbf{x} \int \mathcal{D}\tilde{\mathbf{x}} \exp\left(i \sum_i \int dt \psi_i(t) x_i(t)\right) \exp \sum_i \left(i \int dt (\dot{x}_i(t) - F_i(t, x_1, ..., x_N, \theta), t)) \tilde{x}_i(t))\right), \tag{2.19}$$

which depends also on the parameters θ of the model. The next step consists in averaging over the quenched disorder of these parameters

$$\overline{Z[\psi]} = \int d\theta P(\theta) Z[\psi]. \tag{2.20}$$

As probability distribution $P(\theta)$ is often chosen a Gaussian distribution because of its ubiquitous presence in experimental data in different fields and also because it guarantees the possibility of computing analytically the disorder average (2.20). At this point it is often convenient to introduce some functions or order parameters to write the resulting averaged functional $\overline{Z[\psi]}$ in a compact way. For example, $M(t) = 1/N \sum_i x_i(t)$ can represent the average population abundance in ecological models or the average activity in a neural system at time t. The formal way to introduce these order functions is using the delta-distribution and its integral representation

$$1 = \int \mathcal{D}[M] \prod_t \delta \left(M(t) - \frac{1}{N} \sum_i x_i(t) \right) \tag{2.21}$$

$$= \int \mathcal{D}[\tilde{M}, M] \exp \left(iN \int dt \tilde{M}(t) \left(M(t) - \frac{1}{N} \sum_i x_i(t) \right) \right). \tag{2.22}$$

The choice of these functions depends on the particular system considered and is usually used to explicitly declare the dependence on N of the averaged functional $\overline{Z[\psi]}$ as

$$\overline{Z[\psi]} \propto \int \mathcal{D}[x, \tilde{x}] \int \mathcal{D}[M, \tilde{M}, ...] \exp \left(N \left[... \right] \right), \tag{2.23}$$

where the second integral can be computed, in the thermodynamic limit $N \to \infty$, with the steepest descent method. The optimization procedure for the steepest descent method [45] can also give important relationships for the introduced functions (e.g. $M(t)$). The goal of all these steps is to obtain an effective generating functional Z_{eff} from which one can recognize an effective dynamics. The described procedure is a general receipt, whose application is used in Chapter 3 and Chapter 4 to develop a DMFT respectively for the Generalized Lotka Volterra model and the Rate Recurrent Networks models.

The obtained DMFT consists of an effective Stochastic Differential Equation for an effective agent x of the model that is equivalent in the thermodynamic limit to the initial set of coupled differential equations. The stochastic term follows from the average over the disorder and contains the variability of the different agents of the model. The equivalence between the DMFT and the ODEs in the limit $N \to \infty$ is in a statistical sense, that is, by simulating N effective agents the statistical distributions and properties are equivalent to those of N interacting agents described by the ODEs.

The effective DMFT equations typically depend on the order parameter functions introduced during the derivation procedure (e.g. $M(t)$) that need to be determined by an ensemble average over the realizations of x. Therefore, the complete DMFT consists of the effective equation for x that needs to be solved self-consistently with the definition of the order parameters functions entering in it. This self-consistence cannot usually be solved in close form and need to be solved numerically, at least in the non-stationary regime. An algorithm for this purpose is discussed in the next section. If we consider the stationary version of the DMFT, assuming a convergence to a stationary solution after a transient time, the equations simplify, and the quantities of interest can be expressed as self-consistent (integral) equations depending on the system.

The discussion presented in this section is general and discursive. The exact derivation of the DMFT depends on the details of the system, and practical examples and applications will be discussed in the following chapters of this thesis.

2.5   Numerical Implementation of DMFT

The equations obtained with DMFT are self-consistent since they depend on functions that are averaged over the realizations of the DMFT equation itself, making their solution difficult and computationally expensive. In this section, an algorithm developed by Roy et al. [17] to solve them iteratively

is discussed. Given a self-consistent system of equations composed of a stochastic differential equation SDE that contains observables that are averaged over its realizations $\langle OBS \rangle$, a strategy for the solution can be the following:

Algorithm 1 Strategy for numerical solution of DMFT

    Initialize $\langle OBS \rangle$
    repeat
        Solve N realizations of SDE with current $\langle OBS \rangle$
        Compute new $\langle OBS \rangle$
        Update $\langle OBS \rangle$ with soft injection
    until Convergence

---

where the update with soft-injection of an observable $\mathcal{O}$ is

$$\mathcal{O}_{updated} = (1 - a)\mathcal{O}_{old} + a\mathcal{O}_{new} \tag{2.24}$$

with $0 < a < 1$. The softly reinjection guarantees the convergence of the algorithm independently of the initial conditions [17], and a typical value for a is 0.3.

The iterative Alg. (1) is repeated until convergence or until the maximum number of iterations is reached. To keep track of the convergence it is possible to use the *frobenious* norm of the difference between the updated observable and the ones in the previous iteration and stop the algorithm if all the norms are less than a threshold [17]. A practical implementation will be discussed in Sect. 3.3 for the generalized Lotka-Volterra model and is available in the public repository [46]. Note that the algorithm is computationally very expensive as it scales as $\mathcal{O}(N \times N_{steps}^3)$, where N is the number of DMFT trajectories and N_{steps} is their duration.

Chapter 3

Application to Ecological Models

In this chapter, we explore the application of Dynamical Mean Field Theory in the field of ecology, where the interactions between species and their environment are studied. Over the years, different models of populations dynamics have been studied, starting from the dynamics of a single species, described, for example, with a logistic growth [18] and considering then the interaction between species as done by Lotka and Volterra with their famous predator-prey model [47, 48] or by MacArthur [19] with the Consumer Resource Model. The goal of an ecological model is to capture the type of interactions between species and reproduce the emergent behaviors of the ecosystem. The models mentioned above satisfy the first request to capture the type of interactions, but often fail to reproduce in a quantitative way the patterns of ecological data (sometimes also qualitatively, as shown, for example, by May in the famous complexity-stability discussion [23]). For these reasons, more complicated models have been introduced, such as a generalization of the Lotka-Volterra model [20], where the number of interacting species N and therefore the number of parameters of the model is very large. The Generalized Lotka-Volterra model (GLV) is the archetype of these mathematical models, and most of the methods used in ecology are validated on it. Famous examples are Random Matrix Theory [23], Replica method [11], theory of glasses phases [49], and recently DMFT [24, 50]. The GLV is extensively covered in the literature, and its dynamical behavior as a function of the order parameters of the model is well known [25] and will be discussed in the next sections. In Ref. [24] the DMFT of the random Generalized Lotka-Volterra with quenched disorder is derived and the phase diagram of the system is obtained with a Linear Stability Analysis of the DMFT equation. DMFT has proven to be a versatile tool, as it also yields interesting results in slightly modified GLV models [26, 27].

In this chapter, a saturation function of the interactions is introduced in the GLV model with the aim of removing the unfeasible unbounded growth phase discussed in [25]. We then apply the theoretical tools as done in the literature [13] and the computational algorithm discussed in Sect. 2.5 to derive the phase diagram of this model. As expected, the unbounded growth phase is absent in this version of the GLV, and we are left with a single fixed-point phase (phase I) and a second phase (phase II) that show different behaviors depending on the interaction coefficients, such as multiple attractors or oscillations. We also derive analytically the Species Abundance Distribution (SAD) of this model, which depends on parameters that need to be computed self-consistently. All the theoretical results are validated with simulations of the Ordinary Differential Equations of the GLV for a large number of species.

3.1   Generalized Lotka-Volterra and Saturation of Interactions

In the classical Generalized Lotka-Volterra [21] the interactions between species i with population x_i and species j with population x_j are modeled with the term

$$I_{ij} = \alpha_{ij} x_i x_j. \tag{3.1}$$

If $\alpha_{ij} > 0$ species i benefit from the presence of species j, while if $\alpha_{ij} < 0$ species j is detrimental to i. The linearity of the term I_{ij} in the populations of the species is justified by the fact that, at low density of populations, the probability of encounters is proportional to the populations of both species. The limitations of Eq. (3.1) arises when $x_j \gg x_i$, since it suggests that few individuals of species i are able to interact with all the individuals of the large population of species j, but this is not the case. For this reason we introduce a function $J(x_j)$ of the population x_j with the aim of modeling the saturation of the interactions of species i with species j. Eq. (3.1) becomes

$$I'_{ij} = \alpha_{ij} x_i J(x_j), \tag{3.2}$$

and for the function J we choose

$$J(x_j | K_j) = \frac{x_j}{1 + K_j x_j}, \tag{3.3}$$

where K_j is a parameter of the model that in principle is species dependent. Eq. (3.3) is suitable for our purpose because in the limit $x_j \ll 1$ we get $J(x_j) \simeq x_j$ and Eq. (3.2) gives Eq. (3.1), while if $x_j \gg 1$ we obtain $J(x_j) \simeq 1/K_j$, the saturated interaction. In the following we consider the case $K_j = K$ for all j.

The resulting generalized Lotka-Volterra model is

$$\dot{x}_i = r_i x_i (k_i + \alpha_{ii} x_i + \sum_{j \neq i} \alpha_{ij} J(x_j)), \quad i = 1, .., N \tag{3.4}$$

where the quantities k_i are the carrying capacities, the self interaction terms α_{ii} will be set to -1 and the growth rates r_i to 1. If the interactions are switched off ($\alpha_{ij} = 0 \; \forall i \neq j$) each species will follow a logistic equation $\dot{x}_i = x_i (1 - x_i/k_i)$. We consider the case $k_i = 1$ for all i. Eq. (3.4) becomes

$$\dot{x}_i = x_i (1 - x_i + \sum_{j \neq i} \alpha_{ij} J(x_j)), \quad i = 1, .., N. \tag{3.5}$$

The interaction coefficients α_{ij} and α_{ji} are sampled randomly according to Ref. [25]. For each pair $i < j$ we set

$$\alpha_{ij} = \frac{\mu}{N} + \frac{\sigma}{\sqrt{N}} z_{ij} \qquad \alpha_{ji} = \frac{\mu}{N} + \frac{\sigma}{\sqrt{N}} z_{ji}, \tag{3.6}$$

with $\overline{z_{ij}} = 0$, $\overline{z_{ij}^2} = 1$ and $\overline{z_{ij} z_{ji}} = \gamma$. Operationally, we sample z_{ij} and z_{ji} from a two-dimensional Gaussian distribution with mean $[0, 0]$ and covariance matrix

$$\Sigma = \begin{pmatrix} 1 & \gamma \\ \gamma & 1 \end{pmatrix}, \tag{3.7}$$

and obtain the coefficients α_{ij} and α_{ji} as in Eq. (3.6).

The scale with N of Eq. (3.6) is necessary to obtain a well-defined $N \to \infty$ limit when applying statistical mechanics theory [24]. The parameters μ and σ are, respectively, the average interaction strength and its standard deviation. The parameter $-1 \leq \gamma \leq 1$ characterizes the correlation between the interactions coefficients of a pair of species. If $\gamma = 1$ one has $\alpha_{ij} = \alpha_{ji}$ with probability 1, if $\gamma = 0$ then α_{ij} and α_{ji} are uncorrelated and if $\gamma = -1$ then $\alpha_{ij} = -\alpha_{ji}$. Every time $\alpha_{ij} \alpha_{ji} < 0$ we have a predator-prey pair, therefore, if $\gamma = -1$ the fraction of predator-prey pairs p is $p = 1$. For the fraction $1 - p$ of non-predator-prey pairs, the parameters μ and σ govern the ecological structure by controlling whether the coefficients α_{ij} and α_{ji} are mainly both positive (cooperative interactions) or negative (competitive interactions). In the $N \to \infty$ limit, due to the scaling with N of the coefficients, the $1 - p$ fraction of non predator-prey pairs will be half cooperative and half competitive [24].

In Ref. [25] the phase diagram of the standard GLV is derived as a function of the order parameters μ, σ and γ. The system displays three different dynamical phases: the stable phase, the chaotic phase, and the unbounded growth phase. The introduction of the saturation of the interactions with a limited function $J(x)$ guarantees the removal of the unfeasible unbounded growth of the standard GLV [25].

This result can be shown with a simple argument, at least for a finite number of species N. If the function J is bounded, as for our choice $J(x) < 1/K$, the GLV interaction term $x_i \sum_j \alpha_{ij} J(x_j)$ is also bounded. Defining with a constant M such an upper bound, we can rewrite the right-hand side of Eq. (3.5) as

$$\dot{x}_i \leq x_i(1 + M - x_i) \qquad \qquad \forall i = 1, .., N. \tag{3.8}$$

The upper bound has the functional form of a logistic-equation whose solution is bounded, yielding the proof that there cannot be unbounded growth with the introduction of the function $J(x)$, if K is a finite number different from zero.

3.2   Dynamical Mean Field Theory of GLV

In this section we carry out the Dynamical Mean Field Theory, or Functional analysis, of model (3.5) similarly as done by Galla [24] for the classical GLV. The idea is to consider the limit $N \to \infty$ and use the methods from spin-glasses physics [11, 15, 14] to write a self-consistent stochastic equation equivalent to (3.5). The full details of the derivation can be found in sub-sect. 3.2.1. In Eq. (3.5) we introduce a perturbation field $h(t)$ that is useful to compute dynamical response functions and susceptibilities and will be set to zero at the end of the calculations:

$$\dot{x}_i = x_i(1 - x_i + \sum_{j \neq i} \alpha_{ij} J(x_j) + h(t)), \quad i = 1, .., N. \tag{3.9}$$

We define the dynamical moment generating functional as

$$Z\left[\boldsymbol{\Psi}\right] = \int_{paths} \mathcal{D}\left[\mathbf{x}\right] e^{i \sum_i \int dt J(x_i(t)) \Psi_i(t)}, \tag{3.10}$$

where $\boldsymbol{\Psi} = (\Psi_1, ..., \Psi_N)$ is an external source field. The functional $Z\left[\boldsymbol{\Psi}\right]$ is the Fourier transform of the measure generated by the Lotka-Volterra dynamics. We can constrain the integral over the possible trajectories using a Dirac delta functional and obtain

$$Z\left[\boldsymbol{\Psi}\right] = \int \mathcal{D}\left[\mathbf{x}\right] \prod_i \exp\left(i \sum_i \int dt J(x_i(t)) \Psi_i(t)\right) \times \delta\left(\frac{\dot{x}_i}{x_i} - \left[1 - x_i + \sum_{j \neq i} \alpha_{ij} J(x_j) + h(t)\right]\right). \tag{3.11}$$

Performing an average over the distribution of the coefficients α_{ij} described in the previous Sect. (Eq. 3.6) and evaluating the resulting averaged over disorder functional $\overline{Z\left[\boldsymbol{\Psi}\right]}$ with the saddle point method in the $N \to \infty$ limit we obtain a stochastic differential equation for an effective population $x(t)$

$$\dot{x}(t) = x(t)[1 - x(t) + \gamma \sigma^2 \int_0^t dt' G(t, t') J(x(t')) + \mu Q(t) + \eta(t)]. \tag{3.12}$$

The stochastic process defined by Eq. (3.12) depends on the coloured Gaussian noise $\eta(t)$ that has a temporal correlation

$$C_\eta(t, t') = \langle \eta(t) \eta(t') \rangle = \sigma^2 \langle J(x(t)) J(x(t')) \rangle_x, \tag{3.13}$$

where $\langle \cdot \rangle_x$ is an average over the realizations of Eq. (3.12). In Eq. (3.12) we also find a non-Markovian term characterized by the response function $G(t, t')$ and a term due to the average interaction strength that depends on $Q(t) = \langle J(x(t)) \rangle_x$. The functions $C_\eta(t, t')$, $G(t, t')$ and $Q(t)$ are to be obtained self-consistently as averages over the realizations of the effective-species process, as

$$C_\eta(t, t') = \sigma^2 \langle J(x(t)) J(x(t')) \rangle_x, \tag{3.14}$$

$$G(t, t') = \left\langle \frac{\delta J(x(t))}{\delta h(t')} \right\rangle_x, \tag{3.15}$$

$$Q(t) = \langle J(x(t)) \rangle_x. \tag{3.16}$$

In Sect. 3.3 we implement the iterative Alg. (1) to the DMFT of GLV (3.12) and compare it with the simulations of Eq. (3.5).

Now we focus on long-term behavior and assume the existence of a fixed point $x^* = \lim_{t\to\infty} x(t)$. In the steady state, we see that $\eta^* = \lim_{t\to\infty} \eta(t)$ is a random variable

$$\eta^* = \sigma\sqrt{q}z, \tag{3.17}$$

with

$$q = \left\langle J(x(z))^2 \right\rangle_{P_z(z)}. \tag{3.18}$$

and

$$z \sim P_z(z) = \mathcal{N}(z|0,1). \tag{3.19}$$

The response function $G(t,t')$ at the steady state is time-translation invariant $G(t,t') = G(t - t') = G(\tau)$ and we define

$$\chi = \int d\tau G(\tau). \tag{3.20}$$

We also define

$$Q^* = \left\langle J(x(z)) \right\rangle_{P_z(z)}, \tag{3.21}$$

and find that the stationary limit of Eq. (3.12) is

$$x^* \left[1 - x^* + \mu Q^* + \gamma\sigma^2 \chi J(x^*) + \eta^* \right] = 0. \tag{3.22}$$

Eq. (3.22) has two solutions, the trivial $x^* = 0$ and

$$x^* = \frac{-2t}{Kt - y - \sqrt{(Kt - y)^2 + 4Kt}} H[t], \tag{3.23}$$

with

$$t = 1 + \mu Q^* + \eta^*, \tag{3.24}$$

$$y = 1 - \gamma\sigma^2\chi, \tag{3.25}$$

and $H[t]$ is the Heaviside function expressing the feasibility condition $x^* \geq 0$. The details on the derivation can be found in sub-sect. 3.2.2. We note that in the limit $K \to 0$ Eq. (3.23) yields $x = t/y\, H[t]$ which is the result obtained by Galla [24].

3.2.1 Derivation of DMFT for the GLV with saturation of interactions

In this subsection we derive the DMFT of the GLV with saturation function J according to the procedure described in Sect. 2.4. This subsection can be skipped without loss of continuity.

We start from the generating functional:

$$Z\left[\mathbf{\Psi}\right] = \int_{paths} \mathcal{D}\left[\mathbf{x}\right] e^{i\sum_i \int dt J(x_i(t))\Psi_i(t)}, \tag{3.26}$$

where $\mathbf{\Psi} = (\Psi_1, ..., \Psi_N)$ is an external source field and the integral is computed on the measure generated by the GLV dynamics. We can constrain the integral over the possible trajectories using a Dirac delta functional in its Fourier transform representation and obtain

$$Z\left[\mathbf{\Psi}\right] = \int \mathcal{D}[\mathbf{x}, \hat{\mathbf{x}}] \exp\left(i\sum_i \int dt J(x_i(t))\Psi_i(t) \right) \times$$
$$\times \exp\left(i\sum_i \int dt \hat{x}_i(t) \left(\frac{\dot{x}_i(t)}{x_i(t)} - \left[1 - x_i(t) + \sum_{j\neq i} \alpha_{ij} J(x_j(t)) + h(t) \right] \right) \right). \tag{3.27}$$

Now we can perform the average over the quenched disorder due to the parameters α_{ij}, that are distributed as

$$\alpha_{ij} = \frac{\mu}{N} + \frac{\sigma}{\sqrt{N}} z_{ij} \qquad \alpha_{ji} = \frac{\mu}{N} + \frac{\sigma}{\sqrt{N}} z_{ji}, \tag{3.28}$$

with $\overline{z_{ij}} = 0$, $\overline{z_{ij}^2} = 1$ and $\overline{z_{ij}z_{ji}} = \gamma$. The averaged over disorder functional becomes

$$\overline{Z[\boldsymbol{\Psi}]} = \int \mathcal{D}[P,Q,L,C,K,\hat{P},\hat{Q},\hat{L},\hat{C},\hat{K}] \exp\left(N(\Psi + \Phi + \Omega)\right), \tag{3.29}$$

where we have introduced the order parameters

$$P(t) = i\frac{1}{N}\sum_i \hat{x}_i(t), \tag{3.30}$$

$$Q(t) = \frac{1}{N}\sum_j J(x_j(t)), \tag{3.31}$$

$$C(t,t') = \frac{1}{N}\sum_j J(x_j(t))J(x_j(t')), \tag{3.32}$$

$$L(t,t') = \frac{1}{N}\sum_i \hat{x}_i(t)\hat{x}_i(t'), \tag{3.33}$$

$$K(t,t') = \frac{1}{N}\sum_i \hat{x}_i(t')J(x_i(t)), \tag{3.34}$$

using the Dirac delta representation, e.g. for $L(t,t')$

$$1 = \int \mathcal{D}[L,\hat{L}] \exp\left(iN\int dt\, dt'\hat{L}(t,t')\left(L(t,t') - \frac{1}{N}\sum_i \hat{x}_i(t)\hat{x}_i(t')\right)\right). \tag{3.35}$$

In the argument of the exponential in Eq. (3.29) we have pointed out the dependence on N and we have that Ψ comes from the introduction of the order parameters, Ω depends on the details of the microscopic time evolution and Φ comes from the average over the disorder:

$$\Psi = i\int dt \int dt'\left[\hat{L}(t,t')L(t,t') + \hat{K}(t,t')\hat{K}(t,t') + \hat{C}(t,t')C(t,t')\right] + i\int dt\left[\hat{P}(t)P(t) + \hat{Q}(t)Q(t)\right], \tag{3.36}$$

$$\Omega = \frac{1}{N}\sum_i \log \int \mathcal{D}[x_i,\hat{x}_i]p_0^i(x_i(0)) \exp i\int dt\left(J(x_i(t))\Psi_i(t) + \hat{x}_i(t)\left[\frac{\dot{x}_i(t)}{x_i(t)} - [1 - x_i(t) + h(t)]\right]\right) \times$$

$$\times \exp\left(-i\int dt\, dt'\left[\hat{L}(t,t')\hat{x}_i(t)\hat{x}_i(t') + \hat{C}(t,t')J(x_i(t))J(x_i(t')) + \hat{K}(t,t')\hat{x}_i(t')J(x_i(t))\right]\right) \times$$

$$\times \exp\left(-i\int dt\left[\hat{Q}(t)J(x_i(t))\right]\right) \times \exp\left(-i\int dt\left[\hat{P}(t)i\hat{x}_i(t)\right]\right), \tag{3.37}$$

$$\Phi = -\frac{1}{2}\sigma^2 \int dt\, dt'\left[L(t,t')C(t,t') + \gamma K(t,t')K(t',t)\right] - \mu\int dt P(t)Q(t), \tag{3.38}$$

where $p_0^i(0)$ is the distribution from which the initial values x_i are sampled. Now we are ready to take the limit $N \to \infty$ and compute $\overline{Z[\boldsymbol{\Psi}]}$ with the saddle point. From the optimization of the argument

of the exponential in Eq. (3.29) we obtain the following relations:

$$\mu Q(t) = i\hat{P}(t), \tag{3.39}$$

$$i\hat{Q}(t) = \mu P(t), \tag{3.40}$$

$$\frac{1}{2}\sigma^2 C(t,t') = i\hat{L}(t,t'), \tag{3.41}$$

$$\frac{1}{2}\sigma^2 L(t,t') = i\hat{C}(t,t'), \tag{3.42}$$

$$i\hat{K}(t,t') = \frac{1}{2}\gamma\sigma^2 K(t,t'), \tag{3.43}$$

$$P(t) = \lim_{N\to\infty} \frac{1}{N}\sum_i \langle i\hat{x}_i(t)\rangle_\Omega, \tag{3.44}$$

$$Q(t) = \lim_{N\to\infty} \frac{1}{N}\sum_i \langle J(x_i(t))\rangle_\Omega, \tag{3.45}$$

$$L(t,t') = \lim_{N\to\infty} \frac{1}{N}\sum_i \langle \hat{x}_i(t)\hat{x}_i(t')\rangle_\Omega, \tag{3.46}$$

$$C(t,t') = \lim_{N\to\infty} \frac{1}{N}\sum_i \langle J(x_i(t))J(x_i(t'))\rangle_\Omega, \tag{3.47}$$

$$K(t,t') = \lim_{N\to\infty} \frac{1}{N}\sum_i \langle i\hat{x}_i(t')J(x_i(t))\rangle_\Omega. \tag{3.48}$$

From the normalization constraint of the functional Z it is possible to show that $P(t) = 0\ \forall t$ and $L(t,t') = 0\ \forall t,t'$. Finally, introducing $G(t,t') = -iK(t,t')$ the effective dynamical generating functional is

$$Z_{eff} = \int D[x,\hat{x}]P_0(x(0))\exp i\int dt\hat{x}(t)\left(\frac{\dot{x}(t)}{x(t)} - [1 - x(t) + h(t) + \mu Q(t)]\right)\times$$
$$\times \exp\left(-\sigma^2\int dt\,dt'\left[\frac{1}{2}C(t,t')\hat{x}(t)\hat{x}(t') + i\gamma G(t,t')J(x(t))\hat{x}(t')\right]\right), \tag{3.49}$$

which is the generating functional of the effective dynamics

$$\dot{x}(t) = x(t)[1 - x(t) + \gamma\sigma^2\int dt'G(t,t')J(x(t'))\mu Q(t) + \eta(t) + h(t)], \tag{3.50}$$

with

$$C_\eta(t,t') = \langle\eta(t)\eta(t')\rangle_x = \sigma^2\left\langle J(x(t))J(x(t'))\right\rangle_x, \tag{3.51}$$

$$G(t,t') = \left\langle\frac{\delta J(x(t))}{\delta h(t')}\right\rangle_x, \tag{3.52}$$

$$Q(t) = \langle J(x(t))\rangle_x. \tag{3.53}$$

.

3.2.2 Stationary Solution of Dynamical Mean Field Theory

In this subsection the details of the derivation of the stationary solution of DMFT (3.12) are presented and can be skipped without loss of continuity. Starting from Eq. (3.22) we note that there is a trivial solution $x^* = 0$, and other possible solutions can be obtained by solving the equation

$$1 - x^* + \gamma\sigma^2\chi J(x^*) + \mu Q^*\eta^* = 0, \tag{3.54}$$

with $J(x^*) = x^*/(1 + Kx^*)$. Finally, we have a second degree polynomial equation in x^*. The solutions are

$$x^* = \frac{Kt - y \pm \sqrt{(Kt - y)^2 + 4Kt}}{2K}, \tag{3.55}$$

where we have introduced $t = 1 + \mu Q^* + \eta^*$ and $y = 1 - \gamma \sigma^2 \chi$. The latter is shown to be $y > 0$ in Ref. [24]. Since we want $x^* >= 0$ we need $t > 0$ to have at least one feasible solution. Given that and the fact that $\sqrt{(Kt - y)^2 + 4Kt} \geq |Kt - y|$ we find that the only non-trivial stationary solution is the one with the plus in Eq. (3.55). We also want to consider the case in which $K \to 0$ where Eq. (3.55) is ill-defined when we take the plus sign. To regularize it, it is sufficient to multiply the numerator and the denominator by $Kt - y - \sqrt{(Kt - y)^2 + 4Kt}$. Putting all together the final stationary solution is

$$x^* = \frac{-2t}{Kt - y - \sqrt{(Kt - y)^2 + 4Kt}} H[t]. \tag{3.56}$$

3.3 Comparison of DMFT with GLV simulations

The equations obtained with DMFT are self-consistent since they depend on functions that are averaged over the realizations of the DMFT equation itself, making their solution difficult and computationally expensive. They can be solved by means of iterative algorithms, as discussed in Sect. 2.5. In this section, we implement the iterative algorithm for the DMFT of the GLV model given by Eqs. (3.12, 3.15, 3.14, 3.13). A complete discussion of the procedure can be found in [17]. In particular, this model depends on the functions $Q(t)$, $C_\eta(t, t')$, and $G(t, t')$ that have to be obtained self-consistently. As initialization, we use a random array for $Q(t)$ of length given by the number of time steps that we want to integrate N_{steps}, a symmetric matrix of dimension $N_{steps} \times N_{steps}$ for $C_\eta(t, t')$ and a lower triangular matrix of dimension $N_{steps} \times N_{steps}$ for $G(t, t')$ due to the causality constraint. For the solution of the N realizations of Eq. (3.12) we sample Gaussian paths $\eta(t)$ according to the correlator $C_\eta(t, t')$ and use a simple Euler scheme for integration. The computation of observable $Q(t)$ and $C_\eta(t, t')$ given N realizations of x is straightforward from their definitions (3.14, 3.16). The computation of $G(t, t')$ is instead more complicated because we need to evaluate the variations of $J(x(t))$ with respect to $h(t')$, given the definition (3.15). A possible strategy is to compute $G_i(t, t')$ for each realization x_i of x by integration and then averaging over the realizations. Starting from $J(x_i(t)) = x_i(t)/(1 + Kx_i(t))$ and deriving with respect to $h(t')$ we obtain the following relation:

$$G_i(t, t') = \frac{1}{(1 + Kx_i(t))^2} \frac{\delta x_i(t)}{\delta h(t')}. \tag{3.57}$$

Deriving now with respect to time t keeping t' fixed, with some algebra and substituting Eq. (3.12) we obtain the differential equation

$$\frac{\partial}{\partial t} G_i(t, t') = -2J(x_i(t))G_i(t, t')K[1 - x_i(t) + \gamma \sigma^2 \int_0^t ds G_i(t, s) J(x_i(s)) + \mu Q(t) + \eta_i(t)] +$$

$$G_i(t, t')[1 - 2x_i(t) + \mu Q(t) + \eta_i(t) + \gamma \sigma^2 \int_0^t ds G(t, s) J(x(s))] +$$

$$+ \frac{1}{(1 + Kx_i(t))^2} x_i(t) \gamma \sigma^2 \int_0^t ds G(t, s) G(s, t') + \frac{1}{(1 + Kx_i(t))^2} x_i(t) \delta(t - t'). \tag{3.58}$$

We solve Eq. (3.58) for every $i = 1, .., N$ fixing t' and using a Euler integrator scheme and the initial condition $G_i(t, t') = 0$ for $t < t'$ given by causality. Finally, the estimation of $G(t, t')$ is given by

$$G(t, t') = \frac{1}{N} \sum_i G_i(t, t'). \tag{3.59}$$

The iterative Alg. (1) is repeated until convergence or until the maximum number of iterations is reached as discussed in Sect. 2.5. A similar procedure can be implemented for the stationary solution of DMFT given by Eq. (3.22) in a simpler way since there is no time dependence, meaning that there is no need for Euler integration and the observable Q^*, q, χ are scalars (Eq. 3.21, 3.18, 3.20). As

before, the evaluation of χ requires some calculations. Starting from Eq. (3.20) we see that the time dependence is eliminated and χ is the average over the realizations of $x^* = x(z)$ of the derivative of $J(x(z))$ with respect to $\eta^*(z)$, therefore

$$\chi = \int dz P_z(z) \frac{1}{\sqrt{q}\sigma} \frac{\partial J(x(z))}{\partial z}, \tag{3.60}$$

where $P_z(z) = \mathcal{N}(z|0,1)$. Computing the derivative we obtain

$$\chi = \int_{t>0} dt\, P_t(t) \frac{1}{(1 + Kx(t))^2} f'(t), \tag{3.61}$$

with $t = 1 + \mu Q + \eta$ and $f'(t)$ is the derivative respect to t of the right hand side of Eq.(3.23),

$$f'(t) = \frac{2t\left(K - \frac{4K - 2K(y - Kt)}{2\sqrt{(y-Kt)^2 + 4Kt}}\right)}{(Kt - y - \sqrt{(y-Kt)^2 + 4Kt})^2} - \frac{2}{Kt - y - \sqrt{(y - Kt)^2 + 4Kt}}. \tag{3.62}$$

The code with the implementation of the numerical algorithm for Dynamical Mean Field Theory is available in the public repository [46]. In Fig. 3.1 we show the comparison between the solution of the Generalized Lotka-Volterra model and the corresponding DMFT for different combinations of parameters and the corresponding convergence of the observable to the stationary solution in the numerical implementation of DMFT. Since the simulations of the GLV, as well as the algorithm for the DMFT, are implemented with a finite number of species we note a small discrepancy, especially in the case $\gamma \neq 0$, due to the high computational cost of the observable $G(t, t')$. In fact the scaling of the algorithm in this case is $\mathcal{O}(N \times N_{steps}^3)$.
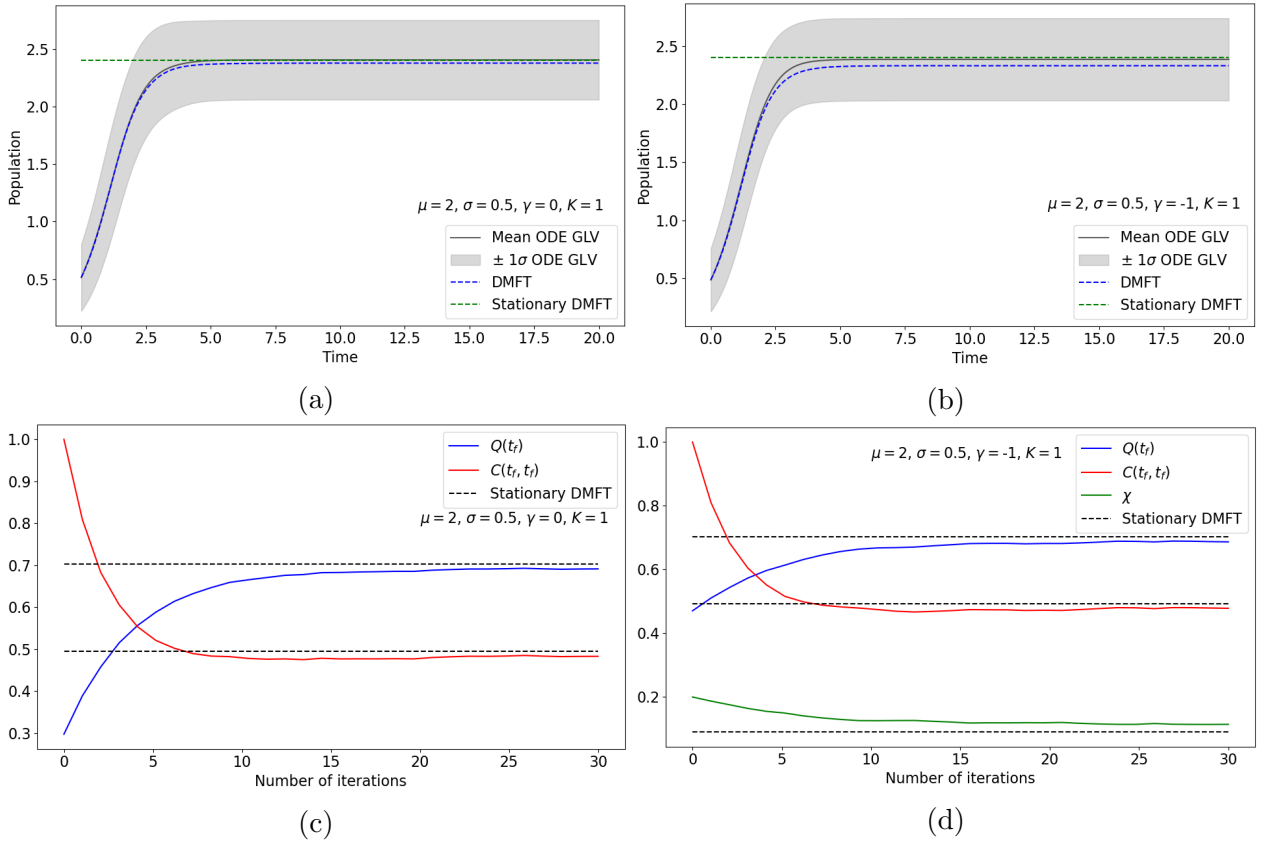

Figure 3.1: Comparison between GLV simulations and DMFT solution for $N = 500$ realizations in the case with $\gamma = 0$ (a) and $N = 200$ realizations for $\gamma = -1$ (b). In (c) and (d) is shown the convergence with the number of iterations of the observable to their stationary solutions. Note that in (c) $\gamma = 0$ and therefore the observable χ is not computed.

3.4 Species Abundance Distribution

In this section we study the species abundance distribution (SAD) for the stationary state of our GLV with saturation of interactions. Starting from the stationary solution of DMFT given by Eq. (3.22) we derive the probability distribution for x^*. We have that $x^* = x^*(t)$ is a random variable function of the random variable t distributed as $t \simeq P_t(t) = \mathcal{N}(1 + \mu Q^*, \sigma^2 q)$. Therefore, the distribution $P_{x^*}(x^*)$ can be obtained as

$$P_{x^*}(x^*) = \langle \delta(x^* - f(t)) \rangle_{P_t(t)}, \tag{3.63}$$

where $f(t)$ is the right hand side of Eq. (3.23), yielding

$$P_{x^*}(x^*) \;=\; \int_{-\infty}^{+\infty} dt \frac{1}{\sqrt{2\pi}\nu} \exp\left(-\frac{(t-m)^2}{2\nu^2}\right) \times \delta\left(x^* - \frac{kt - y + \sqrt{(kt-y)^2 + 4kt}}{2k} H[t]\right), \tag{3.64}$$

where we have introduced the parameters $m = 1 + \mu Q^*$ and $\nu = \sigma\sqrt{q}$ that needs to be computed self-consistently. We can proceed to evaluate the integral by separating the integration interval in $(-\infty, 0]$ and $(0, +\infty)$ to deal with the Heaviside function. From the first subinterval we obtain a Dirac delta $\delta(x^*)$ centered in $x^* = 0$ that multiplies the probability of extinction.

$$P_{ext} = \frac{1}{2}\text{erfc}\left(\frac{m}{\sqrt{2}\nu}\right). \tag{3.65}$$

The second sub-interval can be evaluated exploiting the properties of the Dirac delta distribution and applying the substitution $z = f(t)$, knowing that

$$f^{-1}(z) = z - \gamma\sigma^2\chi J(z). \tag{3.66}$$

The final result for the SAD is

$$P_{x^*}(x^*) = \frac{1}{2}\text{erfc}\left(\frac{m}{\sqrt{2}\nu}\right)\delta(x^*) + \frac{1}{\sqrt{2\pi}\nu}\frac{\exp\left(-\frac{(f^{-1}(x^*)-m)^2}{2\nu^2}\right)}{f'(t)|_{t=f^{-1}(x^*)}}H[x^*], \tag{3.67}$$

where $f'(t)$ is given by Eq. (3.62). In the particular case $\gamma = 0$ we have $y = 1$, $f^{-1}(x^*) = x^*$ and $f'(t) = 1$ resulting in a truncated Gaussian in the second term of Eq. (3.67). Note that Eq. (3.67) depends on the self-consistent parameters q, Q^* and χ and require therefore an iterative procedure for solving the self-consistency. The implementation used in this thesis can be found in the public repository [46]. In Fig. 3.2 we plot the theoretical prediction and the histograms of the simulations obtained by solving the GLV differential equations for different combinations of parameters.
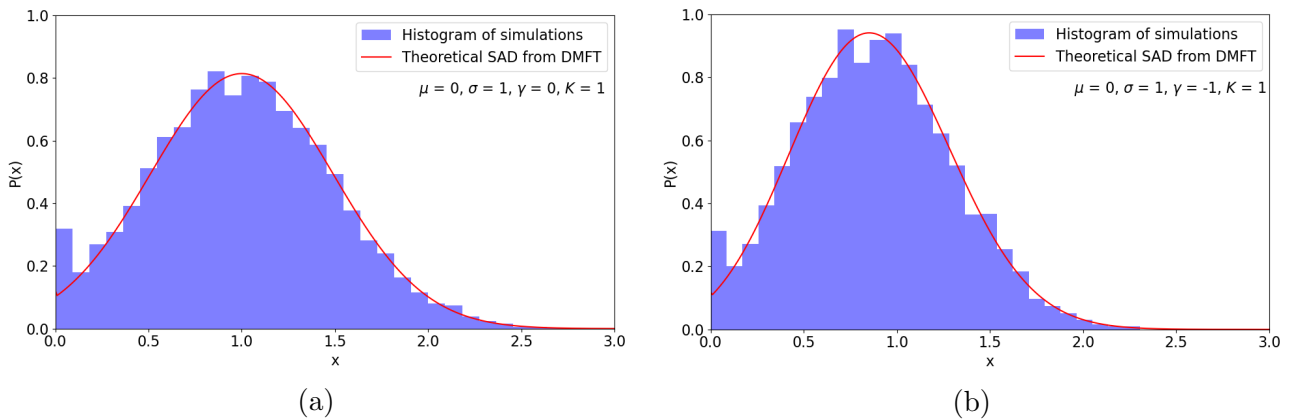

Figure 3.2: Comparison between the histograms of the simulations of GLV with saturation of interactions (25 realizations with $N = 200$ species) with the theoretical SAD prediction for different combinations of parameters.

3.5   Linear Stability analysis and phase diagram

In this section, we study the stability of the stationary solution with a linear stability analysis. We consider the DMFT equation with the external field $h(t)$, which will then be set to zero,

$$\dot{x}(t) = x(t)[1 - x(t) + \gamma\sigma^2 \int_0^t dt' G(t,t') J(x(t')) + \mu Q(t) + \eta(t) + h(t)] \tag{3.68}$$

and its stationary solution x^* given by Eq. (3.23). The linear expansions for η and x are given by

$$\eta'(t) = \eta^* + \delta\eta(t), \tag{3.69}$$
$$x'(t) = x^* + \delta x(t), \tag{3.70}$$

and they have to satisfy Eq. (3.13)

$$\langle \eta'(t)\eta'(t') \rangle = \sigma^2 \langle J(x'(t)) J(x'(t')) \rangle \tag{3.71}$$
$$= \sigma^2 \langle (J'^*)^2 \delta x(t)\delta x(t') \rangle, \tag{3.72}$$

with $J'^* = (\partial J/\partial x)|_{x=x^*}$ and using $\delta J(x) = \delta x(t) J'^*$. The linearized DMFT equation is

$$\delta\dot{x}(t) = \delta x(t)[1 - x^* + \gamma\sigma^2 \chi J(x^*) + \mu Q^* \eta^*] + x^*[-\delta x(t) + \gamma\sigma^2 \int dt' [\delta G(t,t') J(x(t')) +$$
$$+ G(t,t')\delta J(x(t') + \mu\delta Q(t) + \delta\eta(t) + \delta h(t)], \quad (3.73)$$

and it is easy to show that $\delta G(t,t') = 0$ and $\delta Q(t) = 0$ starting from their definition and showing that it can be written as the average of an unperturbed observable and δh. Given the independence between the two and the fact that $\langle \delta h \rangle = 0$ the term mentioned above is zero. Therefore, if we consider the above simplifications and the trivial stationary solution $x^* = 0$ we obtain

$$\delta\dot{x}(t) = \delta x(t)[1 + \mu Q^* + \eta^*], \tag{3.74}$$

that is stable if $t = 1 + \mu Q^* + \eta^* < 0$ and unstable otherwise. For the non trivial stationary solution the equation for linear perturbations becomes

$$\delta\dot{x}(t) = x^*[-\delta x(t) + \gamma\sigma^2 \int dt' G(t,t')\delta J(x(t')) + \delta\eta(t) + \delta h(t)]. \tag{3.75}$$

We apply now the Fourier transform on both sides, obtaining

$$i\omega\delta\tilde{x}(\omega) = x^*[-\delta\tilde{x}(\omega) + \delta\tilde{\eta}(\omega) + \delta\tilde{h}(\omega) + \gamma\sigma^2 \tilde{G}(\omega)\delta\tilde{x}(\omega) J'^*], \tag{3.76}$$

and solving for $\delta\tilde{x}(\omega)$ we get

$$\delta\tilde{x}(\omega) = A(\omega)^{-1}[\delta\tilde{\eta}(\omega) + \delta\tilde{h}(\omega)], \tag{3.77}$$

with

$$A(\omega) = \left[\frac{i\omega}{x^*} + 1 - \gamma\sigma^2 \tilde{G}(\omega) J'^*\right]. \tag{3.78}$$

Since δh is chosen to be a Gaussian noise, we have

$$\langle \delta\tilde{h}(\omega)\delta\tilde{h}(\omega') \rangle = \epsilon^2 \delta(\omega + \omega') 2\pi, \tag{3.79}$$

where ϵ is the strength of the Gaussian noise. Regarding $\langle \delta x(t)\delta x(t') \rangle$, since we are around the fixed point it depends only on $t - t'$, and therefore

$$\langle \delta\tilde{x}(\omega)\delta\tilde{x}(\omega') \rangle = \epsilon^2 \delta(\omega + \omega') 2\pi\delta\tilde{C}(\omega), \tag{3.80}$$

where $\delta\tilde{C}(\omega)$ can be obtained from Eqs. (3.77, 3.80, 3.79, 3.71). The final result is

$$\delta\tilde{C}(\omega) = \left[\left\langle \frac{1}{B(\omega,\omega')} - (J'^*)^2\sigma^2 \right\rangle\right]^{-1}, \tag{3.81}$$

where $B(\omega, \omega') = A(\omega)^{-1} A(\omega')^{-1}$ and the $\langle \cdot \rangle$ is an average over the distribution of x^*, with $x^* > 0$. We are in particular interested in the long time response and we therefore consider $\omega = \omega' = 0$. We obtain that in this case

$$B(0,0) = \frac{1}{(1 - \gamma \sigma^2 \chi J'^*)^2}, \tag{3.82}$$

and that $\delta \tilde{C}(0)$ diverges if the following critical condition is satisfied

$$1 = \phi \sigma^2 \int_{x^*>0} dx^* P(x^*)(J'^*)^2 \frac{1}{(1 - \gamma \sigma^2 \chi (J'^*))^2}, \tag{3.83}$$

with $\int_{x^*>0} dx^* P(x^*) = 1$, ϕ being the fraction of non-extincted species and $J'^* = \frac{1}{(1+Kx^*)^2}$. We note that taking the parameter $K = 0$ in Eq. (3.3) we have $J(x) = x$ and $J'(x) = 1$, and the critical condition becomes $(1 - \gamma \chi \sigma^2)^2 - \phi \sigma^2 = 0$ which is the same result obtained by Galla [24] for the standard GLV.

Eq. (3.83) can be solved self-consistently with the SAD distribution (3.67) and the self-consistent parameters χ, Q^* and q given by the Equations (3.20, 3.21, 3.18). A possible Python implementation of a solver of the resulting system of integral equations can be found in the public repository [46]. In Figs. 3.3, 3.4, 3.5 we plot the critical line obtained from solving Eq. (3.83) for different combinations of the control parameters of the model. The critical line separates two phases: the stable phase I (at
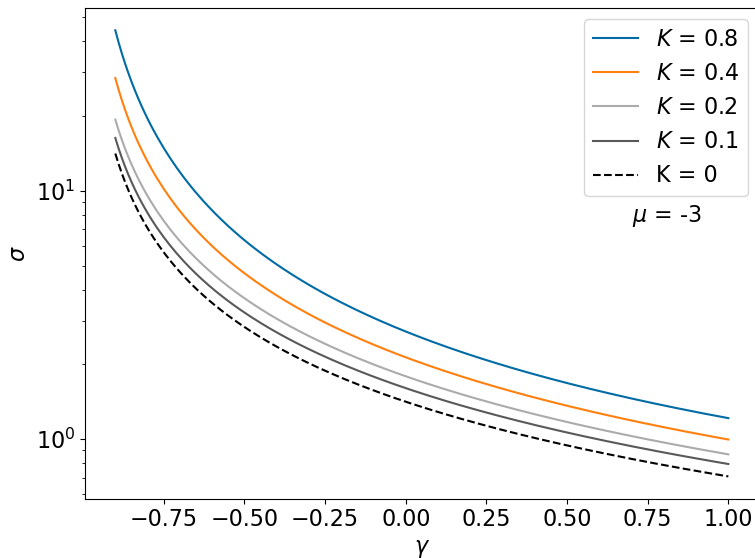

Figure 3.3: Plot of the critical line in the γ-σ plane of the Generalized-Lotka-Volterra model with saturation function obtained by solving self-consistently the stability condition (3.83).

the bottom) with a unique fixed point and the chaotic phase 2 (at the top) with multiple attractors and oscillatory behavior. The validity of the results has been validated with numerical simulations, as will be discussed in the next section. In Fig. 3.3 is shown that with a lower value of γ, that is, a higher fraction of predator-prey interactions, the critical value of σ is higher and the system is more stable. In particular, for $\gamma = -1$ (total asymmetric case) there is a divergence, and only a stable phase with a unique fixed point is possible. Moreover, increasing the parameter K makes the system more stable, as expected by the higher level of saturation. In the limit $K \to 0$ the results known in the literature are found. In Fig. 3.5 the μ-σ phase diagram is shown. As previously, the stability of the system increases with K and for $K \to 0$ it approaches the known result $\sigma_c = \sqrt{2}$, when $\mu \leq 0$. Note that for $\mu > 0$ in the case $K = 0$ the unbounded growth phase appears but cannot be determined with this analysis. In Fig. 3.5 the same phase diagram is shown, but for different values of γ. As discussed above, with lower γ the system is more stable owing to a higher fraction of predator-prey pairs. We also note that the trend of the critical line is monotonic, increasing with the average interaction μ, suggesting that cooperative interactions stabilize the system more than competitive interactions.
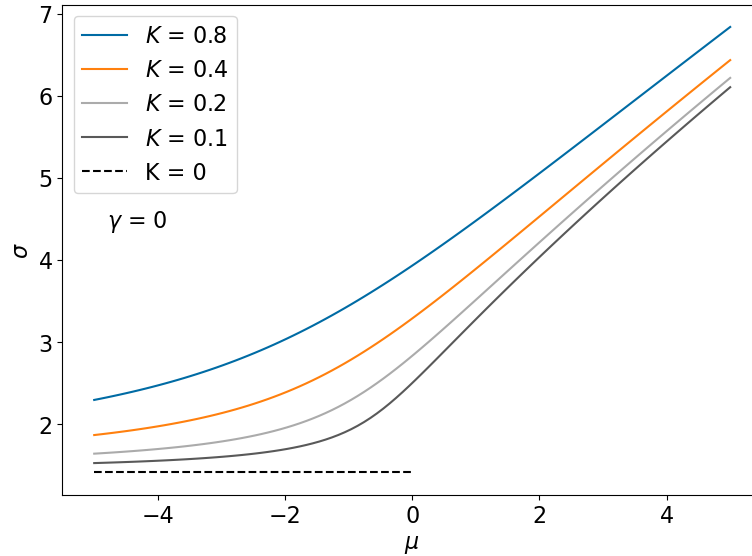
Figure 3.4: Plot of the critical line in the μ-σ plane of the Generalized-Lotka-Volterra model with saturation function for different values of K obtained by solving self-consistently the stability condition (3.83).
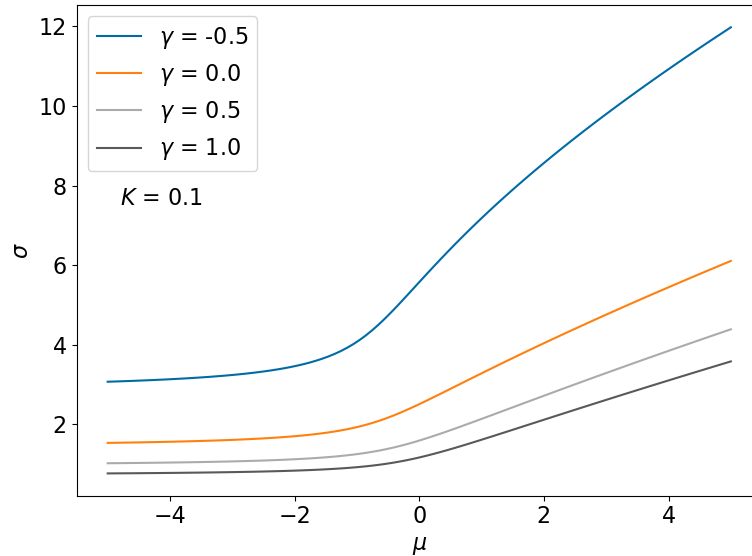

Figure 3.5: Plot of the critical line in the μ-σ plane of the Generalized-Lotka-Volterra model with saturation function for different values of γ obtained by solving self-consistently the stability condition (3.83).

3.6 Numerical simulations and validation of the phase diagram

In order to validate the results obtained with Linear Stability Analysis of the DMFT we produce some simulations of the GLV model with saturation function (3.5). Firstly, we verify that the unfeasible unbounded growth phase is eliminated by the introduction of the saturation function J by testing a large number of diversified sets of control parameters of the model with $K \neq 0$. This was expected as discussed in Sect. 3.1. Secondly, we want to show that the critical line predicted in the previous section actually separates two different phases, a stable phase I with a Unique Fixed Point and a chaotic phase II with unstable behavior. To rigorously distinguish the behavior of a dynamical system, one should compute the Lyapunov exponents of the system, which is not trivial in the case of a GLV system. In this thesis, we have implemented a more intuitive and less rigorous argument following [26]. The idea is to introduce some order parameters that can distinguish phase I from phase II. The main qualitative difference between the two phases is that in phase I, given any initial condition, we expect the system to stabilize at a unique fixed point while this is not true when the system is in phase II. In the unstable phase, we expect the system to either not reach a stable stationary point or to stabilize
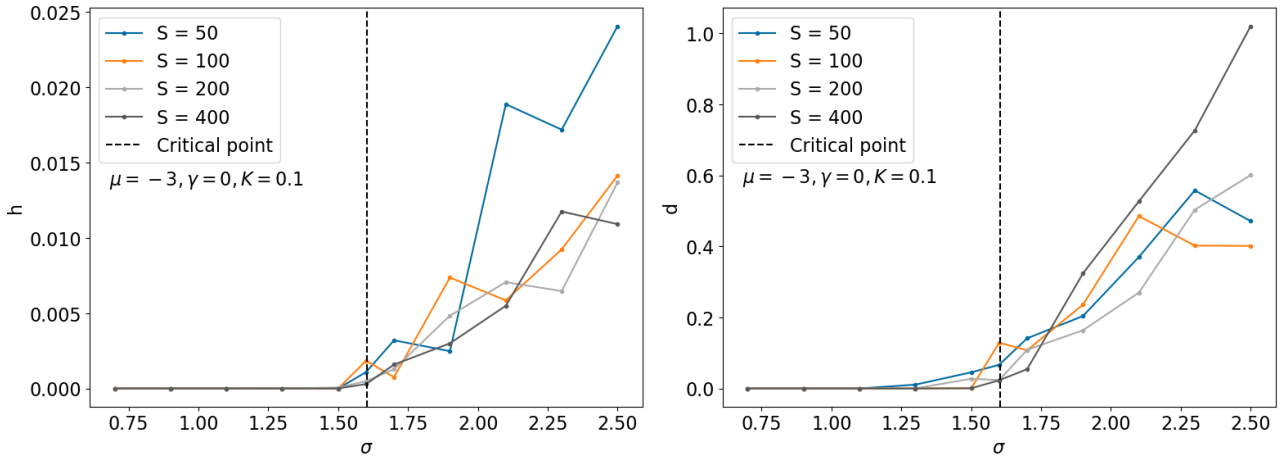
Figure 3.6: Plot of the order parameters h and d obtained by simulating the GLV system with saturation function at different values of σ, fixing $\mu = -3$, , $\gamma = 0$, $K = 0.1$. The dashed line represents the critical value of σ obtained solving self-consistently Eq. (3.83).

at different fixed points depending on the initial conditions. For this reason, we have introduced two order parameters: h which measures fluctuations in the dynamics of the system and d which measures the distance between two simulations run with the same interaction matrix α but with different initial conditions. The two order parameters are defined as

$$h = \frac{\langle \langle x_i(t)^2 \rangle_T - \langle x_i(t) \rangle_T^2 \rangle_N}{\langle \langle x_i(t) \rangle_T^2 \rangle_N}, \tag{3.84}$$

$$d = \frac{\langle \langle (x_i(t) - x_i'(t))^2 \rangle_N \rangle_T}{\langle \langle x_i(t) \rangle_N^2 \rangle_T}, \tag{3.85}$$

where $\langle \cdot \rangle_N$ is the average over the different populations, $\langle \cdot \rangle_T$ is the average over the last 5% time steps of the trajectories and x_i' is a second simulation obtained using the same interaction matrix but different initial conditions. In Fig. 3.6 we plot the values of the order parameters h and d obtained from the simulations where we have fixed the parameters μ, γ and K of the model varying σ. We compare it with the critical value σ_c obtained solving Eq. (3.83) and we observe that the order parameters h and d are null where we expect phase I and different from zero in the chaotic phase. This correspondence between predictions and simulations is systematically found for different values of the control parameters of the system. From Fig. 3.6 we note also that considering a higher number of species S yields a more robust result for the behavior of the system. This is a consequence of the fact that the transition between the two phases is sharp only in the limit $S \to \infty$, while at a finite number of species S the transition fades. For this reason, the number of repetitions of simulations required to have robust results is very large. Fig. 3.6 is obtained sampling 100 different interaction matrices. We have therefore showed that the Linear Stability Analysis of the DMFT yields a critical condition to determine the transition from stability to instability that is consistent with numerical simulations. However, it does not give any insight into the behavior of the system in phase II and does not exclude the possibility of different chaotic phases. In this thesis, we have explored numerically the qualitative behavior of the chaotic phase by changing the parameter γ and we have observed that two different qualitative behaviors can be appreciated. When the parameter γ is small, the system behaves in a volatile way, while when γ is sufficiently large it seems to have multiple-marginally stable fixed points. Examples of these dynamics of the systems can be found in Fig. 3.7 and Fig. 3.8. A possible way to distinguish the two different chaotic phases is to use the previously defined order parameter h and d. In particular, we expect both h and d to be different from zero in the volatile phase while we expect $h = 0$ in the multiple-fixed-points phase because the populations do not fluctuate around the stationary point. In Fig. 3.9 we plot the value of the parameters h and d varying γ and, as expected, we observe $h = 0$ and $d = 0$ when $\gamma < \gamma_c$, that is, when the system is in the stable phase, while both become different from zero when transitioning into the chaotic phase. In particular, when γ is increasing and
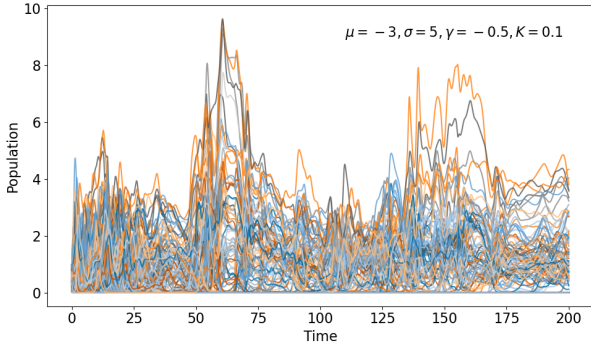
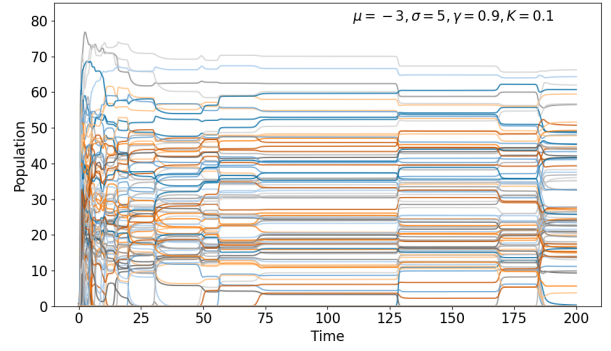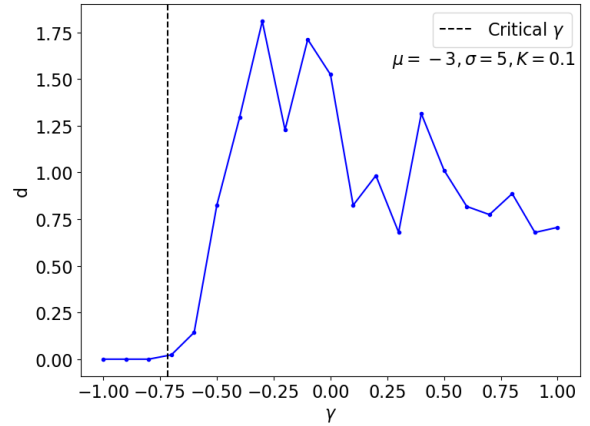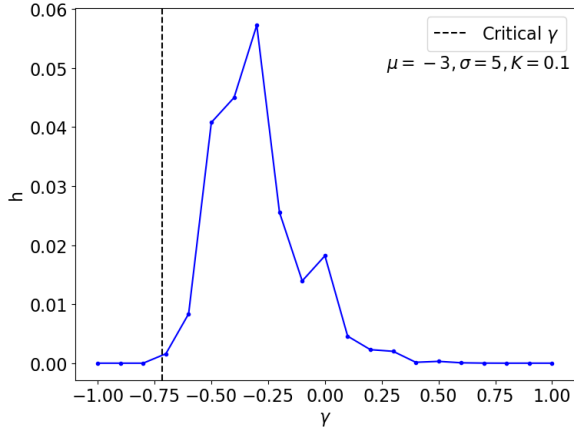Figure 3.7: Example of chaotic phase with volatile behavior.

Figure 3.8: Example of chaotic phase with multiple-fixed-points.

Figure 3.9: Order parameters h and d as a function of the parameter γ and comparison with the prediction of the critical value of γ (dashed line).

tends to 1, the parameter h becomes small again, suggesting a sort of transition from volatile behavior to multiple-fixed-points behavior. However, it is not clear if the different behavior is caused by a sharp phase transition obtained changing the parameter γ or a smooth change in the qualitative behavior of the chaotic phase that may depend on the symmetry and antisimmetry properties of the stability matrix of the GLV model (3.5) and the consequent properties of its spectrum. We note also that a similar behavior in the chaotic phase is observed also in Ref. [26] where they have modified the GLV model introducing a non-linear feedback to the interactions. The similarity between our work and their results suggests that the emergent patterns that we have observed could be a general qualitative consequence of having an upper bound for the interaction term of the GLV that is independent of the specific form of the bound and in particular of the functional form of $J(x)$, as long as this function saturates. All these suggestions are, at this level, speculations, based on the discussed observations and we leave their, probably non-trivial, investigation for future works.

22

Chapter 4

Application to Neural Systems

One of the most complex systems in nature is the brain. For this reason, life sciences and especially neuroscience are a very rich field to investigate. In this chapter, we investigate an application of recurrent neural networks in the field of theoretical neuroscience, borrowing the notation from [51]. The brain is composed of $\sim 10^{11}$ neurons, each of them is connected with $\sim 10^3$ synapses to other neurons for a total of $\sim 10^{14}$ connections. For this reason, the study of its structure and functions usually focuses on a particular scale that is compatible with the interest of the research. Depending on the goal, one can start with single neurons [52] and scale up to culture of neurons [53], neural circuits [54], and whole brain models [55]. Here, we focus our attention on neural circuits. The purpose of our work is to investigate the heterogeneity of the autocorrelation time distributions observed in many neural circuits [32, 56]. This heterogeneity of timescales forms a reservoir that appears to have a fundamental role in the resolution of complex tasks in primate [57] and artificial neural networks [33]. In Chapter 5 we investigate empirically the autocorrelation times of mouse olfactory bulbs. The analysis shows that the histogram of the samples of the autocorrelation time at rest, that is, during spontaneous activity, is a skewed distribution with a fat tail (Fig. 5.10). Note that in this thesis, the autocorrelation times are estimated as the Half Width at Half Maximum (HWHM) of the autocorrelation function. In this chapter, we focus on the theoretical aspects of this investigation, starting from the work of Stern, Istrate, and Mazzucato [36]. In their work, they propose a simple model that naturally generates a reservoir of timescales [36]. The model will be discussed in detail throughout this chapter, but we anticipate here that the fundamental idea is to introduce a recurrently connected network of heterogeneous neural assemblies. Neuronal assemblies are collections of neurons that show highly correlated activity in cortical circuits and are often referred to as ensembles [58]. The key idea of the model is to assume that these assemblies are heterogeneously distributed, in accordance with experimental observations [37, 59]. This hypothesis and the interplay of criticality are discussed as basic mechanisms to generate the observed reservoir of timescales.

4.1 E-I Spiking Networks and Rate Networks

In this section we briefly introduce two important models in theoretical neuroscience: the Excitatory and Inhibitory (E-I) spiking networks [60] and the rate networks of neural assemblies [51]. The first model is the more biologically driven of the two, but it is very difficult to treat analytically. It is typically used for simulations and validation of analytical results [61]. The second model is a sort of coarse-grained empirical version of the E-I spiking network, as shown in Fig. 4.1, that tries to capture the essential features of neural circuits simplifying the overall complexity of the model.

In the E-I spiking networks, the nodes of the networks are neurons that are connected recurrently. Neurons can be excitatory (E) or inhibitory (I), and the fraction of neurons per type is usually fixed in the network. Excitatory neurons promote the generation of an electrical signal, whereas inhibitory neurons prevent it. This is encoded in the model with a positive out-coupling for excitatory neurons and a negative out-coupling for inhibitory neurons. In the network weights are also encoded the

assemblies, as couplings of neurons within the same assembly are chosen to be stronger than couplings between neurons belonging to different assemblies. This encoding strategy is plausible from a biological point of view, since according to the definition of functional ensembles [58] the activity of neurons within the same ensemble is highly coordinated and from the hebbian principle [62], *neurons that fire together, wire together*, we expect their connections to be stronger than other random couplings. The dynamics of this E-I spiking network is usually computed with the integrated and fire neurons procedure [63] and the dynamical variable is the current. A simple representation of this model is shown in Fig. 4.1 on the left, and more details can be found in [61, 36].

We now introduce the rate networks with neural assemblies following [36]. In this model, the nodes of the network represent neural assemblies that are recurrently connected. We interpret the unit self-coupling as proportional to the assembly size, that is, the number of neurons belonging to that ensemble. This is justified by the result obtained in [61, 36], where a mean-field procedure is applied to the E-I spiking networks, obtaining a model that is very similar to the rate network considered here.
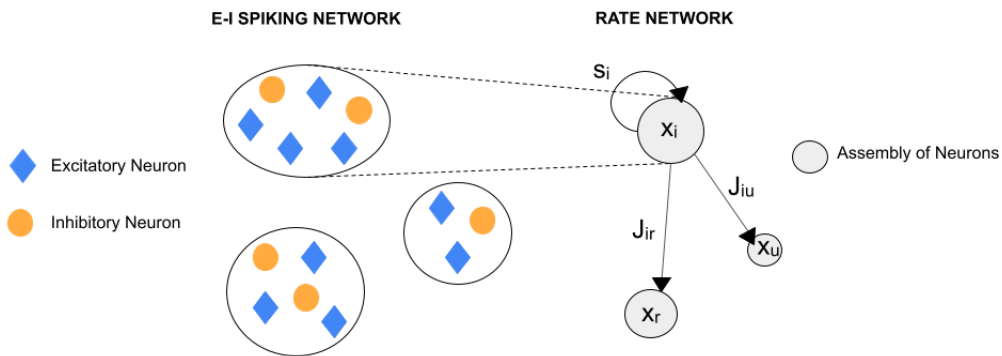

Figure 4.1: Figure inspired from [36]. Left: Spiking network of excitatory and inhibitory cells arranged in assemblies of different sizes. Right: Coarse-grained phenomenological model based on recurrent networks of rate units, with self-coupling s_i and interaction coupling J_{ij} with other units. The self-coupling s_i is proportional to the size of assembly i.

The dynamics of this rate-network model is governed by the dynamical equations

$$\frac{dx_i}{dt} = -x_i + s_i\phi(x) + g\sum_{j=1}^{N} J_{ij}\phi(x_j) \quad i = 1, ..., N \tag{4.1}$$

where the random couplings J_{ij} from unit j to unit i are drawn independently from a Gaussian distribution with mean 0 and variance $1/N$, g represents the network gain and we use the transfer function $\phi(x) = \tanh(x)$. Self-couplings s_i are drawn from a distribution $P(s)$ on a support S that can be discrete or continuous and represent the size of the assembly i. This distribution can be chosen in different ways, leading to different features of the system as will be discussed in Sect. 4.3. Note that Eq. (4.1) is an equation for the currents in each assembly x_i, but can be considered as an equation for the rates since these are easily recovered with the transfer function $\phi(x_i)$. The rates obtained with the transfer function are a sort of normalized min-max rates around the baseline, and therefore assume values in $[-1, 1]$ instead of the classical positive values.

4.2 Dynamical Mean-Field Theory of Assembly Rate Networks

Given the model defined by Eq. (4.1), it is possible to carry out the Dynamical Mean Field Theory in the limit $N \to \infty$, with the procedure described in Sect. 2.4 and similarly as done in Sect. 3.2 for the GLV systems. The details of the calculations can be found in [36], which is based on the original work of [14]. The average over the quenched disorder is applied to the couplings J_{ij}, while the average over the self-couplings s_i cannot be applied since, depending on the choice of their distribution $P(s)$, their

specific value can heavily influence the dynamics of the unit [36]. The final self-consistent equations for units x_α with self-coupling $s_\alpha \in S$ are

$$\frac{dx_\alpha}{dt} = -x_\alpha + s_\alpha \phi(x_\alpha) + \eta(t). \tag{4.2}$$

We denote by N_α the number of units with self-coupling s_α and with $n_\alpha = N_\alpha/N$ the corresponding fraction. The mean field $\eta(t)$ is the same colored Gaussian noise for all units, with mean $\langle \eta(t) \rangle = 0$ and autocorrelation

$$\langle \eta(t)\eta(t+\tau) \rangle = g^2 C(\tau), \tag{4.3}$$

$$C(\tau) = \sum_{\alpha \in A} n_\alpha \langle \phi\left[x_\alpha(t)\right] \phi\left[x_\alpha(t+\tau)\right] \rangle, \tag{4.4}$$

where $\langle \cdot \rangle$ is the average over realizations of Eq. (4.2) and we have indexed with $\alpha \in A$ the possible values of the self-couplings s_α. In the case where the self-couplings distribution $P(s)$ is continuous, it is easy to extend the results by replacing the sum in Eq. (4.4) with an integral,

$$\langle \eta(t)\eta(t') \rangle = g^2 \int p(s)\phi[x(s,t)]\phi[x(s,t')]ds, \tag{4.5}$$

with $p(s)$ the density function of the self-couplings and $x(s,t)$ the dynamic variable obeying to

$$\frac{d}{dt}x(s,t) = -x(s,t) + s\phi[x(s,t)] + \eta(t). \tag{4.6}$$

In the next subsections, we present the standard methods introduced by [34, 35, 36] to compute the fixed points of the DMFT of the rate networks given by Eq. (4.2) and a stability criterion for them based on random matrix theory [64].

4.2.1 Fixed Points

The computation of fixed points for the DMFT of Rate Networks with neural assemblies [36] is a generalization of the one introduced in [35] for a rate network with constant self-coupling $s_i = s$ for all units. Fixed points are obtained by solving self-consistently the static version of equations (4.2, 4.4), that is, solving

$$x_\alpha - s_\alpha \phi(x_\alpha) = \eta \qquad \forall \alpha \in A, \tag{4.7}$$

where the mean-field η is a Gaussian random variable with zero mean and its variance is given by

$$\langle \eta^2 \rangle = g^2 C, \tag{4.8}$$

$$C = \sum_{\alpha \in A} n_\alpha \langle \phi[x_\alpha]^2 \rangle. \tag{4.9}$$

Given Eq. (4.7), the solution for each unit depends on s_α. Once the standard deviation of η is obtained self-consistently, for each unit, a random Gaussian number η is sampled and Eq. (4.7) can be solved numerically. A geometric representation of the solutions for two different cases, $s_\alpha < 1$ with only one solution and $s_\alpha > 1$ with three solutions, is shown in Fig. 4.2.

4.2.2 Stability condition and transition to Chaos

The study of the stability of the fixed points of DMFT of rate networks with neural assemblies is a generalization by [36] of the procedure introduced in [35]. The idea is to expand the dynamical equation (4.1) around the fixed points computed from the DMFT Eq. (4.7), as described in the previous subsection, to obtain a stability matrix M. The analysis of the properties of the eigenvalues of M leads to a stability criterion given by the request that all the eigenvalues have a negative real
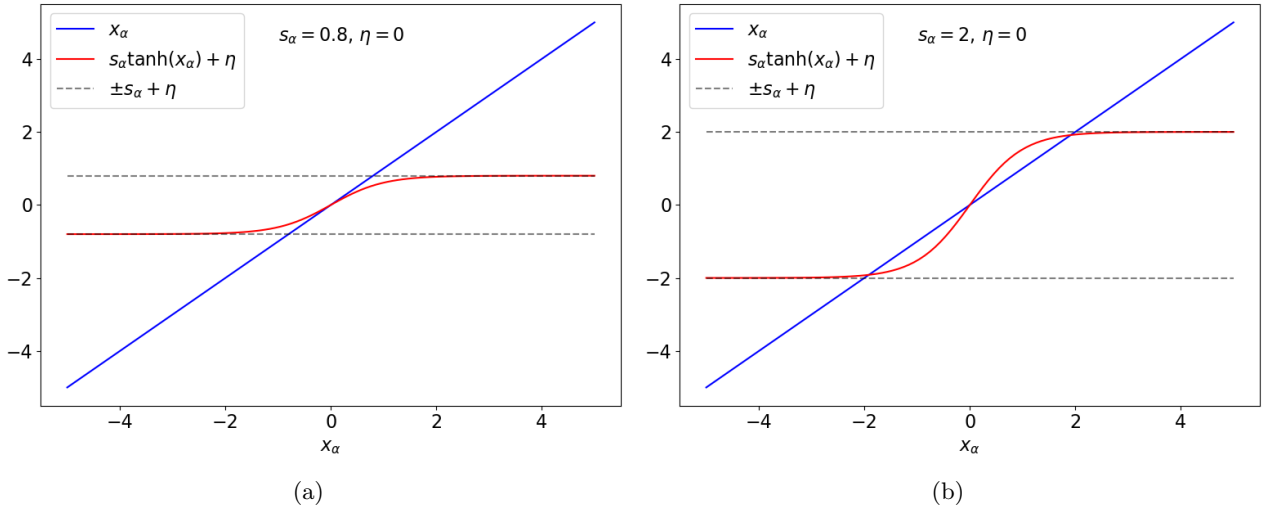
Figure 4.2: (a) Example of geometric solution of Eq. (4.7) for $s_\alpha < 1$. At most one solution is possible depending on the value of the sampled η. (b) Example of geometric solution of Eq. (4.7) for $s_\alpha < 1$. At most three solutions are possible, depending on the value of the sampled η.

part. The following results are based on the groundwork on Random Matrix Theory done in [64]. From [35, 64], an eigenvalue of the stability matrix exist at a point z in the complex plane if

$$g^2 \sum_{\alpha \in A} n_\alpha \left\langle \frac{\phi'(x_\alpha)^2}{[z + 1 - s_\alpha \phi'(x_\alpha)]^2} \right\rangle > 1. \tag{4.10}$$

We note that the denominator is given by z added to the slope of the left hand side (LHS) of Eq. (4.7), hence if a solution x_α^* of Eq. (4.7) gives a negative slope (available when $s_\alpha > 1$) leads to a vanishing value of the denominator in some positive z and to a positive eigenvalue and instability [36]. Another compact way to write the stability condition is obtained considering that a fixed-point solution becomes unstable as soon as an eigenvalue occurs at $z = 0$, which happens when

$$g^2 \sum_{\alpha \in A} n_\alpha \langle q_\alpha^{-1} \rangle \leq 1, \tag{4.11}$$

where $q_\alpha = [s_\alpha - \cosh^2(x_\alpha)]^2$. The stability condition (4.11) can be solved numerically and self-consistently with Eq. (4.7) to obtain the phase line transition from stable fixed points to chaos. An application of the procedure introduced in this sub-section is shown in Sect. 4.3.2.

4.3 Weak, Constant and Heterogeneous Self-couplings

The rate network model defined by Eq. (4.1) and the corresponding DMFT (4.2) are general and depend on the choice of the distribution of the Self-Couplings distribution $P(s)$. In this section, we summarize the historical evolution of the choice for $P(s)$ and present the three most interesting choices: weak or negligible self-couplings $s_i \ll 1$ studied in [34], constant and non-negligible self-coupling $s_i = s \ \forall i$ studied in [35] and heterogeneous distribution of self-couplings introduced by [36]. In this investigation, we are interested in identifying the dynamical behaviors of the systems, with particular attention to the individuation of the critical transition from stability to chaos for the different choices. In the chaotic phase, we are interested in the autocorrelation functions and times, inspired by the seminal work of Ginzburg and Sompolinsky [31]. These are estimated as Half-Width at Half-Maximum (HWHM) of the autocorrelation function $C(\tau)$ given by Eq. (4.4) for the DMFT and by the standard definition

$$C_x(\Delta t) = \int dt' \left[x(t') - \langle x \rangle \right] \left[x(t' + \Delta t) - \langle x \rangle \right], \tag{4.12}$$

26

for the dynamical Eq. (4.1). The HWHM estimator is chosen for the autocorrelation times instead of the standard decay time of the fitted exponential because, especially in the experimental data, the autocorrelation functions do not display an exponential behavior as shown in Chapter 5.

4.3.1 Weak or Zero Self Couplings.

The first case to be analyzed is the one in which self-couplings are assumed to be zero or weak ($\mathcal{O}(1/N)$) and was first studied in [34]. In this case, there is only one DMFT equation (effective for all units) given by

$$\frac{dx}{dt} = -x + \eta(t), \tag{4.13}$$

with the mean-field noise defined as usual, $\langle \eta(t)\eta(t')\rangle = g^2\langle \phi[x(t)]\phi[x(t')]\rangle$. In this case, it is simple to obtain the stability condition from the DMFT results described in the previous Sect. 4.2.2. The fixed points are simply given by $x = \eta$, where η is a Gaussian random variable with zero mean and variance given by Eq. (4.8). Therefore, since the distribution of x in this case is a Gaussian distribution with zero average and the hyperbolic cosine appearing in Eq. (4.11) is an even function, the stability condition (4.11) becomes

$$g \leq 1. \tag{4.14}$$

The resulting phase diagram is:

- $g < 1$ results in a *zero fixed point phase*, where x converges to zero for all initial conditions (*silent phase*);

- $g > 1$ results in a *chaotic phase* that can display limited cycles or oscillations around zero [34].

In the original paper [34], the analytical results are carried out by rewriting the dynamical equations in terms of differential equations for the autocorrelation of the variable x, $\Delta(\tau) = \langle x(t)x(t+\tau)\rangle$, which is connected to the autocorrelation function $C(\tau)$ by the relation $\Delta - \ddot{\Delta} = C$. In this case, autocorrelations can be computed analytically as well as the maximal Lyapunov exponent [34], which is obtained by introducing the response function $\chi_{ij}(t,t') = \partial x_i(t)/\partial x_j(t')$. As expected, the maximum Lyapunov exponents λ are less than zero if $g < 1$ and greater than zero if $g > 1$, confirming the results obtained with the DMFT. In the limit $N \to \infty$, the transition from silence to chaos is sharp [34]. In Fig. 4.3 three different examples of dynamics for this case ($s = 0$) are shown, with different values of network gain g. For $g = 0$, as expected, an exponential decay is obtained, while for $g = 1$, long transients and oscillations are observed at the critical point, and for $g = 2$ the expected chaotic behavior is observed.

4.3.2 Constant Self-Couplings

The case in which all the self-coupling are equal and of the order of one, that is, $s_i = s \simeq \mathcal{O}(1)$ $\forall i = 1, ..., N$ is studied in [35]. In this case, simulations, DMFT and stability analysis reveal that the system can display a silent phase and a chaotic phase as in the previous case, but also a multiple fixed points with transient chaos depending on the parameters of the model. The model (4.1) in this case is reduced to

$$\frac{dx_i}{dt} = -x_i + s\phi(x_i) + g\sum_{j\neq i} J_{ij}\phi(x_j) \qquad i = 1, ...N \tag{4.15}$$

in which the control parameters are the size of the assemblies s and the gain parameter g. We start with a brief analysis of the simple special cases of this model. If $s = 0$ we get back the previous model [34] with a silent phase if $g < 1$ and a chaotic phase if $g > 1$. If, instead, $g = 0$, we obtain a system of uncoupled neurons, whose fixed points are determined by the equation $x = s\phi(x)$. For $s < 1$ the only solution is $x = 0$, that is, we have a silent phase, while if $s > 1$ there are two non-zero solutions that are negatives of each other. In the last case, each neuron shows bi-stability, and since we have N independent neurons the system has 2^N stable fixed points. Non-zero values of s and g give rise to interesting interplay between chaos and bi-stability [35]. In Fig. 4.4 some examples of dynamical simulation of the model for different values of the order parameters s and g are shown. We note that
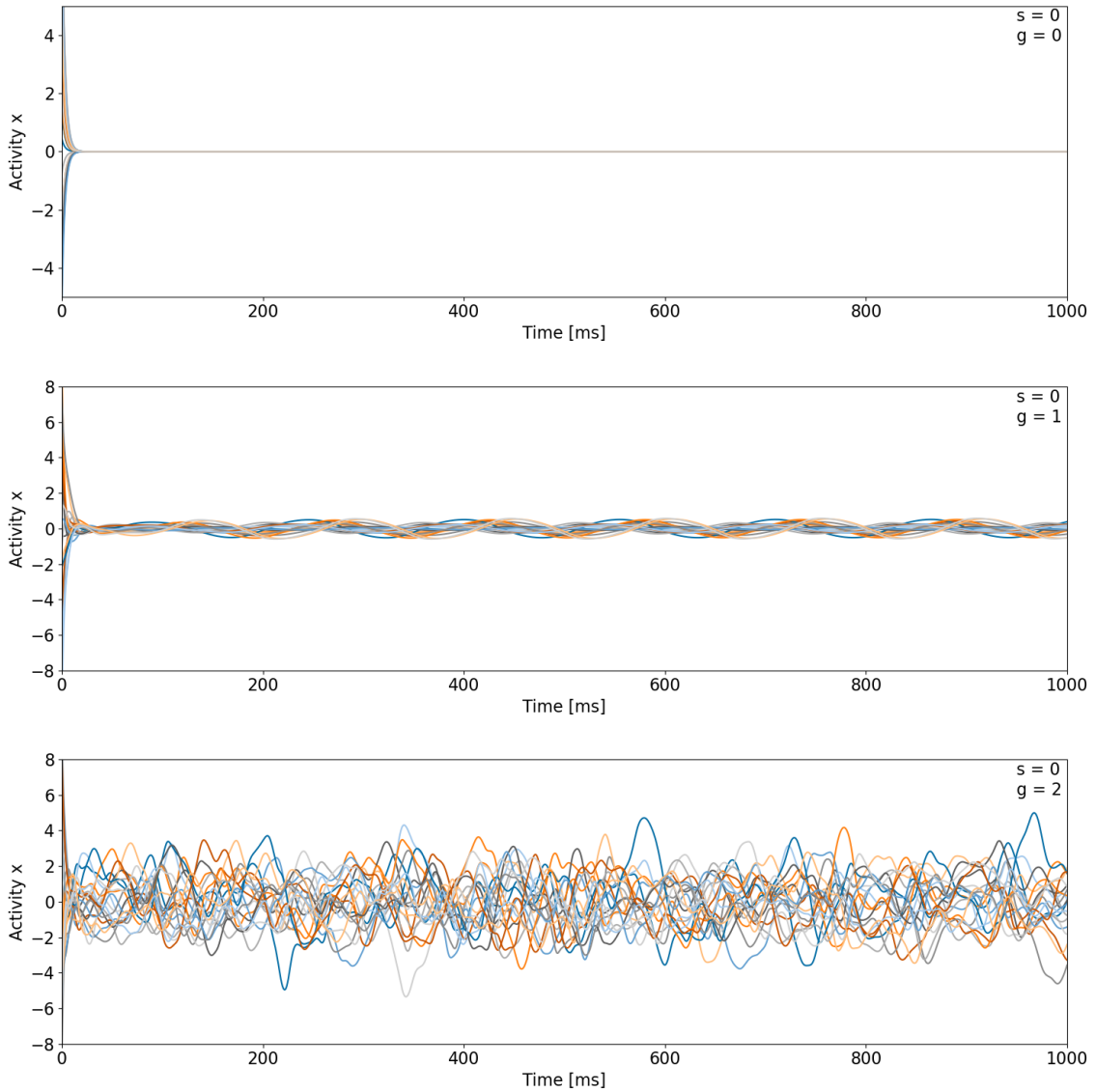
Figure 4.3: Different examples of dynamics with weak self-interaction $s = 0$. The plot presents 20 random units of simulations with $g = 0$ at the top (no-interaction), $g = 1$ at the center (critical point) and $g = 2$ at the bottom (chaotic phase). The simulations have been run with 400 units and the time is converted to milliseconds using a membrane timescale of 3 ms.

for small values of g we observe a silent phase for small s and multi-stability for large s. Increasing the value of g we observe longer chaotic transients and chaotic behavior.

We proceed now to apply the theory developed in Sect. 4.2 to study the phase diagram of rate networks with constant self-coupling, following [35]. The DMFT (4.2) in this case consists of only one equation (one effective population with self-coupling s)

$$\frac{dx}{dt} = -x + s\phi(x) + \eta(t), \tag{4.16}$$

and the autocorrelation of the Gaussian noise (4.4) is

$$C(\tau) = \langle \phi\left[x(t)\right]\phi\left[x(t+\tau)\right]\rangle. \tag{4.17}$$

We start by considering the trivial zero fixed point $x_i = 0 \; \forall i$, that is, the silent phase. The stability matrix of the model, obtained by computing the Jacobian of Eq. (4.15) in $x_i = 0$ and $x_j = 0$, is in this case
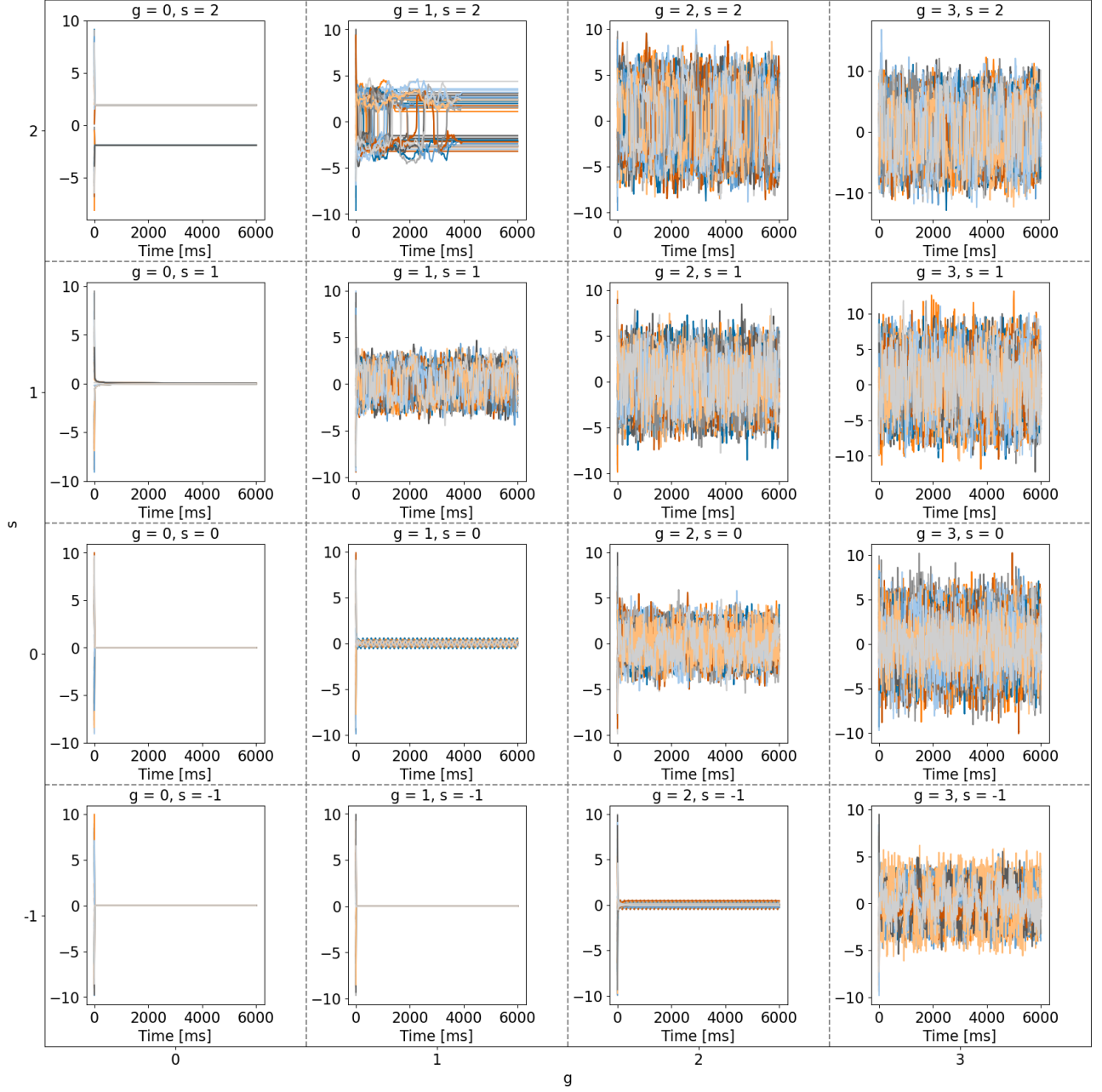
$$M_{ij} = (-1 + s)\delta_{ij} + gJ_{ij}.$$

Figure 4.4: Plot of random units activity for different simulations with different parameters g and s. The plots presents the activty of 10 sampled neurons within 5 different simulations of 400 neurons. The time is converted in milliseconds assuming a membrane time constant of $3ms$. The behavior of the simulations is compatible with the one predicted in the theoretical phase diagram in Fig. 4.5.

J is a random matrix whose eigenvalues lie in a circle of unit radius for large N [65]. For M, the radius is multiplied by a factor g and shifted by an amount $(-1 + s)$. The final stability condition is therefore

$$-1 + s + g < 0. \qquad (4.18)$$

The non-zero fixed points are obtained by solving the static version of the DMFT (4.16),

$$x - s\phi(x) = \eta \qquad (4.19)$$

and are random variables $x = x(\eta)$. If $s \neq 0$, this must be solved numerically and yields three possible solutions if $s > 1$ [35]. The stability matrix in this case is

$$M_{ij} = \delta_{ij}\left(-1 + s\left[\phi'(x_j)\right]\right) + gJ_{ij}\phi'(x_j), \qquad (4.20)$$

29

where, since $\phi(x) = \tanh(x)$, its derivative is $\phi'(x) = 1 - \tanh^2(x)$. The fixed point is stable if the eigenvalues of M have all real parts less than zero. Ref. [35] evaluates M using the mean-field solutions $x(\eta)$ as described in Sect. 4.2. By applying Eq. (4.10) is easy to show that in the limit $N \to \infty$ the matrix M has an eigenvalue at the point z in the complex plane if

$$\int_{-\infty}^{+\infty} D_\sigma \eta \left(\frac{g\phi'[x(\eta)]}{|z + 1 - s\phi'[x(\eta)]|} \right)^2 > 1, \tag{4.21}$$

where

$$D_\sigma \eta = \frac{d\eta}{\sqrt{2\pi}\sigma} \exp\left(-\frac{\eta^2}{2\sigma^2}\right). \tag{4.22}$$

This result is derived based on the groundwork of [64], but does not support isolated eigenvalues [64]. It is better to consider Eq. (4.11), which expresses if there is an eigenvalue at $z = 0$

$$Q = \int_{-\infty}^{+\infty} D_\sigma \eta \left(\frac{g}{\cosh[(x(\eta)]^2 - s} \right)^2 > 1. \tag{4.23}$$

The stability condition therefore becomes $Q \leq 1$, with the edge of stability defined by $Q = 1$ [35]. We are assuming that the edge of stability is when there is an eigenvalue at $z = 0$. Equation (4.23) can be solved self-consistently and numerically with the fixed point equation $x - s\phi(x) = \eta$, knowing the distribution of η given by (4.22), exploiting the symmetry of the problem $\eta \to -\eta$ and acknowledging that the solution $x = 0$ is unstable as the denominator of equation (4.21) is zero at a real positive value of z [35]. According to [35], an approximated form for the critical line is given by

$$s_c(g) = 1 + 0.157 \log(0.443g + 1), \tag{4.24}$$

that yields the critical value of s for a given g. The phase diagram obtained considering the critical lines given by Eq. (4.18) and Eq. (4.24) is shown in Fig. 4.5.
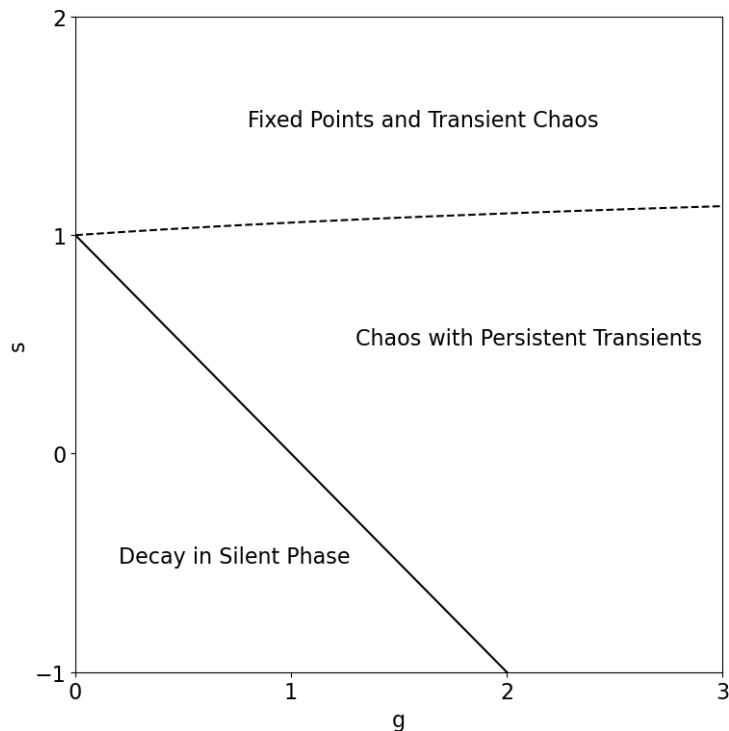

Figure 4.5: Phase diagram of Rate Network with constant self-coupling s. The solid line separates the silent phase with activity that decays to zero from the chaotic phase. The dashed line separates the two chaotic phases: the one with persistent transient at the bottom and the one with long-transients (exponential in the number of units N) at the top.

4.3.3 Heterogeneous Self-Couplings

Until now, only one constant value of self-coupling s has been considered, either equal to zero (Sect. 4.3.1) or different from zero (Sect. 4.3.2). In this section, we consider a different choice for the self-couplings. According to the experimental results [37, 59], the sizes of the functional ensembles in cortical circuits are heterogeneously distributed, with fat tails. With this in mind, we explore the introduction of a lognormal distribution for self-couplings $P(s) = \log \mathcal{N}$, as done in [36]. The lognormal distribution is a continuous distribution of a variable whose logarithm is normally distributed, that is, if X is log-normally distributed, then $Y = \log X$ has a normal distribution. The probability distribution function is

$$P(X|\mu, \sigma) = \frac{1}{x\sigma\sqrt{2\pi}} \exp\left(-\frac{(\log x - \mu)^2}{2\sigma^2}\right), \tag{4.25}$$

where μ and σ are respectively the mean and the standard deviation of the random variable $Y = \log X$. The mean and variance of the lognormal variable X are given by:

$$Mean(X) = \exp\left(\mu + \frac{\sigma^2}{2}\right), \tag{4.26}$$

$$Var(X) = \left[\exp(\sigma^2) - 1\right]\exp\left(2\mu + \sigma^2\right). \tag{4.27}$$

An example of log-normal distribution is shown in Fig. 4.6, which is the same distribution used for self-couplings in the following analysis.
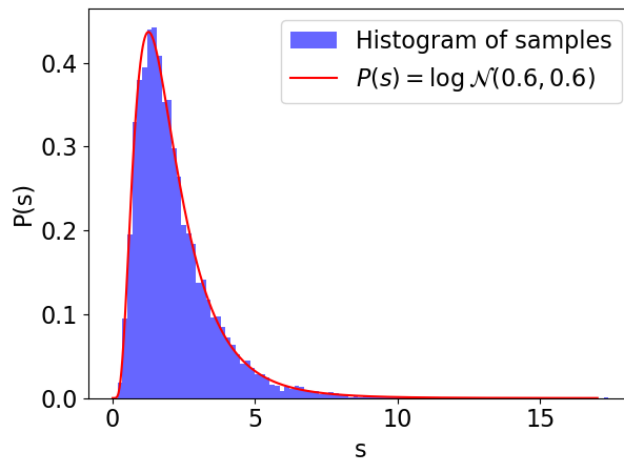

Figure 4.6: Histogram of samples of self-coupling s_i and comparison with the corresponding log-normal distribution $P(s) = \log \mathcal{N}(0.6, 0.6)$.

As anticipate in Sect. 4.2, for continuous distributions of $P(s)$, Eq. (4.4) becomes

$$\langle \eta(t)\eta(t')\rangle = g^2 \int P(s)\phi[x(s,t)]\phi[x(s,t')]ds, \tag{4.28}$$

and the DMFT equation becomes

$$\frac{d}{dt}x(s,t) = -x(s,t) + s\phi[x(s,t)] + \eta(t). \tag{4.29}$$

Note that in this case we interpret $P(s)$ as a density function of the self-coupling distribution s. With this choice of self-couplings, it is not possible to analytically predict the transition from stable fixed points to chaotic behavior. In Fig. 4.7, some examples of simulations for different values of the gain network g are shown. Similarly to the previous cases, for small g we observe one stable fixed point, while increasing g the transient before convergence becomes longer and longer until the chaotic phase is reached.
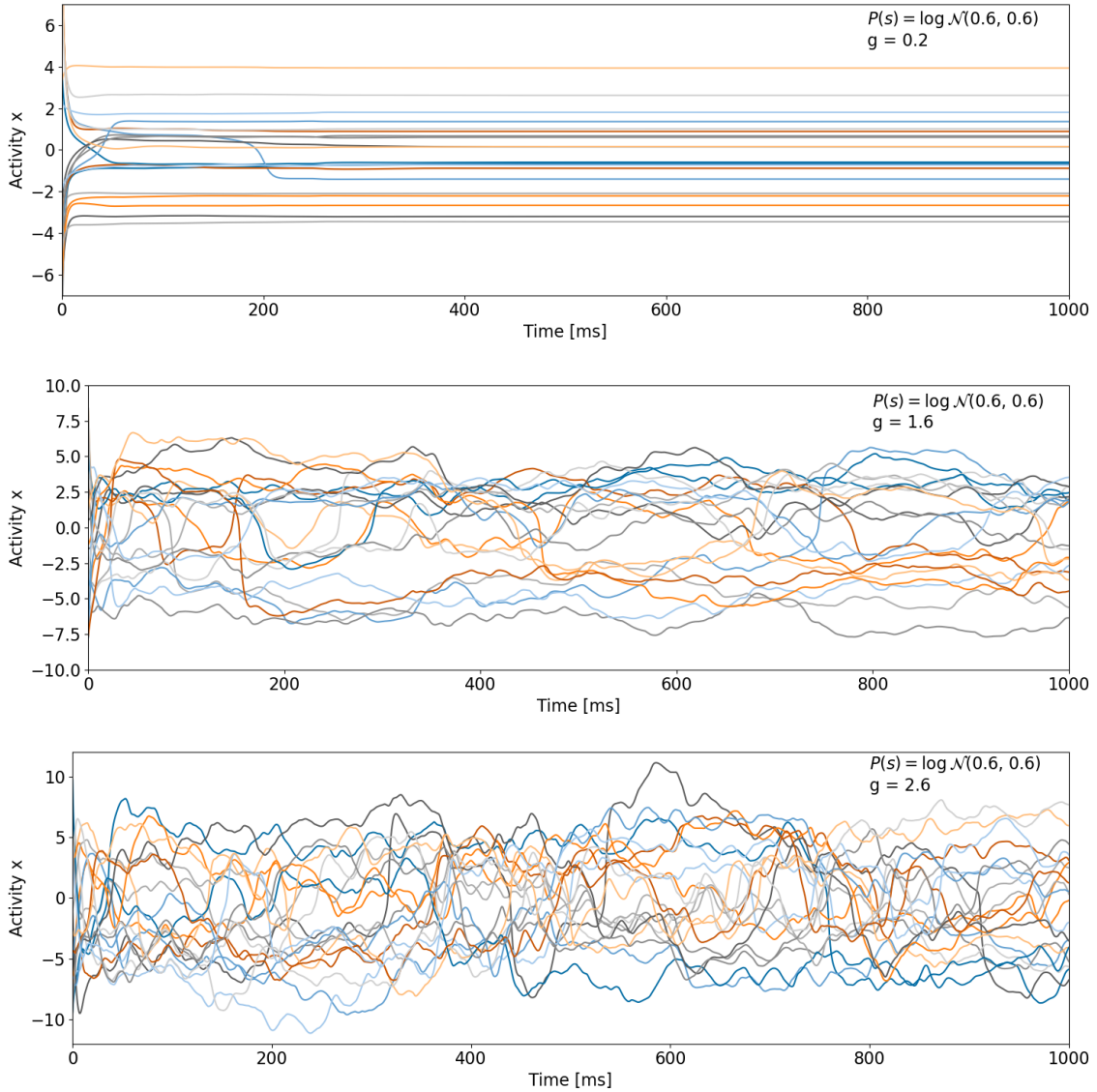
Figure 4.7: Different examples of dynamics with heterogeneous distribution of self-couplings s, sampled from a lognormal distribution $P(s) = \log \mathcal{N}(0.6, 0.6)$. The plot presents 20 random units of simulations with $g = 0.2$ at the top (fixed-point phase), $g = 1.6$ at the center (near the critical point) and $g = 2.6$ at the bottom (chaotic phase). The simulations have been run with 400 units and the time is converted to milliseconds using a membrane timescale of 3 ms.

4.4   Timescales heterogeneity

The mechanisms that generate the heterogeneity of timescales observed in the experimental data [32, 66] are yet unknown. In this section, we study the autocorrelation times of the simulations of the models introduced above as the Half Width at Half Maximum (HWHM) of the autocorrelation function of the activity of the single assembly, computed according to the definition (4.12). Following [36], we show here that the introduction of heterogeneity in self-couplings naturally generates a reservoir of timescales. In Fig. 4.8 a scatter plot of self-couplings s_i and the corresponding autocorrelation times τ_i is shown. As expected, the histogram of the self-couplings s_i (at the top of the figure) is compatible with the designed distribution. Interestingly, the histogram of the autocorrelation times τ_i also exhibits a heterogeneous distribution. The system is chosen to be in the chaotic phase by using $P(s_i) = \log \mathcal{N}(0.6, 0.6)$ as the self-coupling distribution and $g = 2$ that is large enough to be in the chaotic phase. In order to further investigate the importance of heterogeneity in the self-couplings for the emergence of the reservoir of timescales we investigate with some simulations how the dynamical behavior of the system influences it, that is, how relevant is the presence of chaos or criticality in the
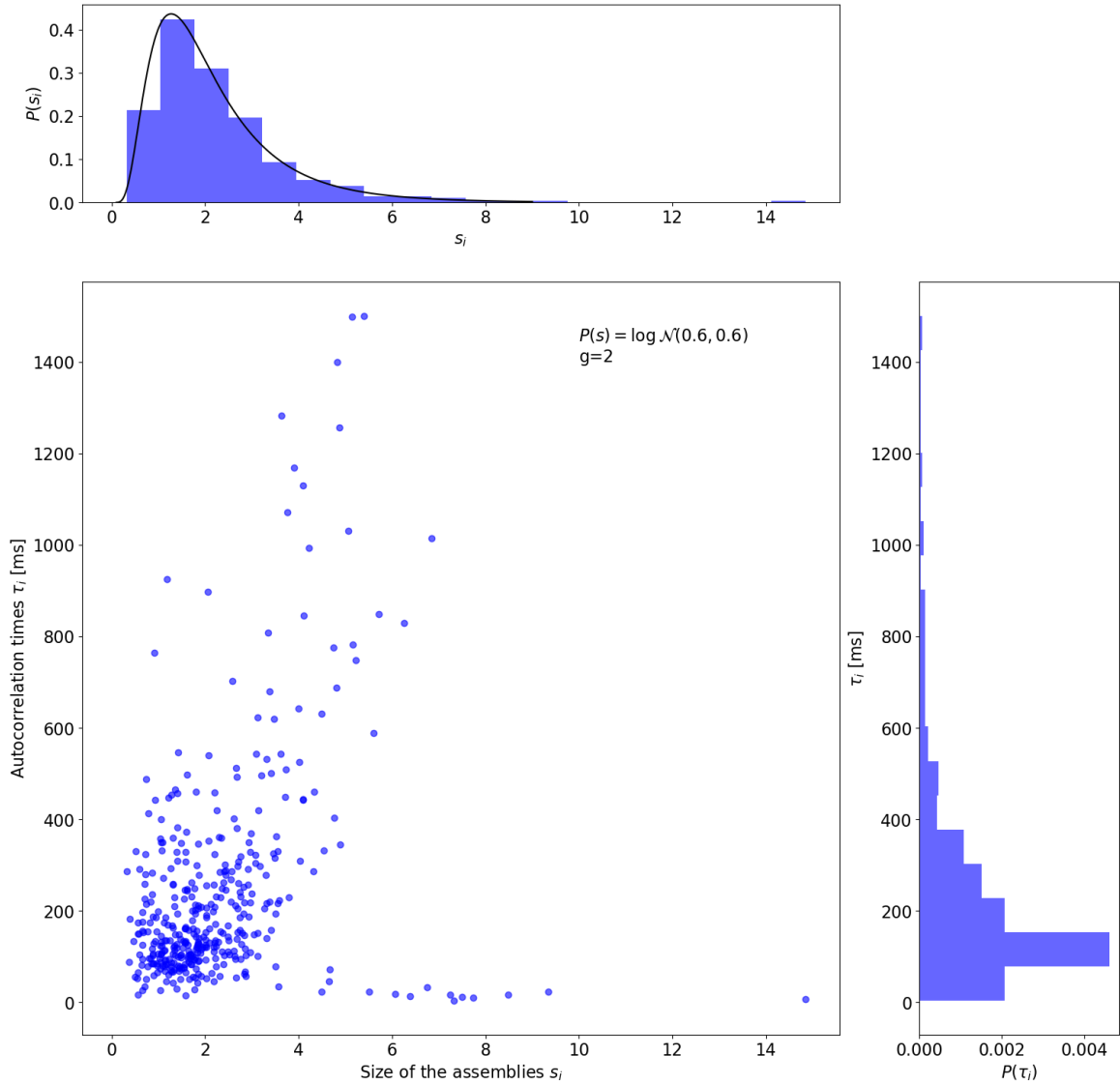
32

Figure 4.8: Scatter plot of self-couplings and corresponding auto-correlation times for a random simulation with self-coupling distribution $P(s) = \log \mathcal{N}(0.6, 0.6)$ (at the center) and histograms of the auto-correlation times (at the right) and self-couplings (at the top). The times are converted in ms using a membrane time constant of 3 ms.

dynamics of the system for the emergence of the above mentioned pattern. We proceed in computing repeated simulations (20 runs for every set of parameters) with 400 units with different choices for the model parameters. We start by considering as above a lognormal distribution of self-couplings with parameters $\mu = 0.6$ and $\sigma = 0.6$ and we change the value of the gain network g, from 0.4 to 3.0. We repeat the same simulations imposing that all assemblies have the same self-coupling $s = 2.2$, which is similar to the mean of the lognormal distribution chosen in the first run $\langle s \rangle \simeq = 2.2$. For every node of every simulation we compute the autocorrelation time of the activity and collect together the ones obtained with the same model parameters. We then compute the standard deviation of such collections and use this parameter as a measure of the width of the reservoir of timescales generated by the models for every choice of parameters. Another possibility, suggested in [35] was to compute the average autocorrelation function for every choice of model parameters and compute its HWHM. The results of our simulations are shown in Fig. 4.9. From Fig. 4.9 it is evident that both the case with constant self-couplings and heterogeneous self-couplings displays a bump of the standard deviation of the autocorrelation times near the critical point. The critical point, highlighted with a dashed line, has been validated by visual inspection of the simulations. Another important result, shown in Fig. 4.9, is that the bump near the critical point in the case of constant s is very thin while in the case
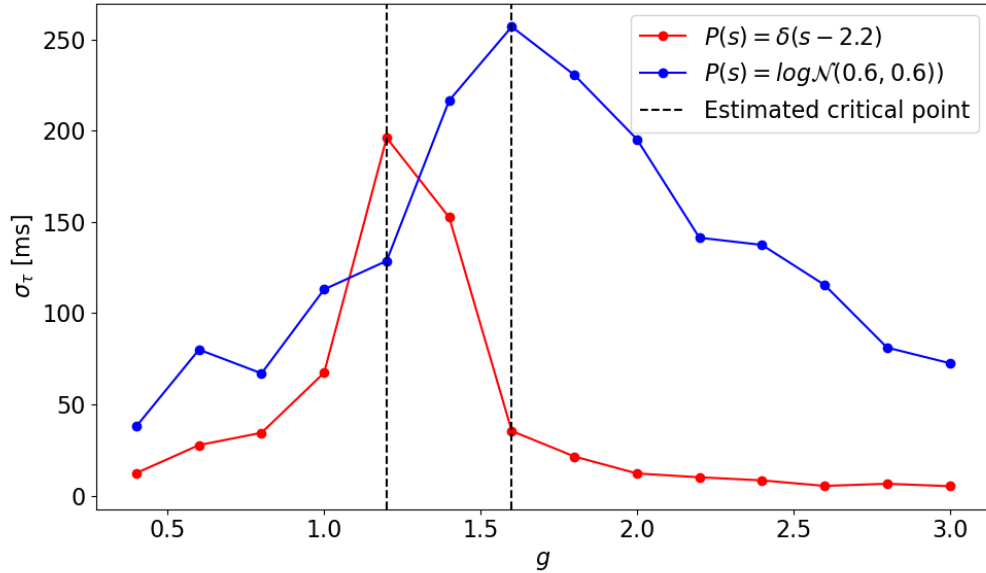
Figure 4.9: Plot of the standard deviation of the distribution of autocorrelation times as a function of g for two different self-coupling distribution: $P(s) = \delta(s - 2.2)$ and $P(s) = \log \mathcal{N}(0.6, 0.6)$. Note that the mean value of the lognormal distribution is $\simeq 2.2$, which is the value of s chosen for the constant distribution with a Dirac-delta.

of heterogeneous self-couplings is much wider. Combining these observations, the simulations suggest that the baseline mechanism for the generation of a reservoir of timescales could be the criticality of the system, and not the heterogeneity of the self-couplings. It is although clear that, in the case of constant s, the window in which the emergence of the reservoir of timescales is observed is very tiny, while, assuming heterogeneity of self-couplings, the window of in which we expect the reservoir of timescales around the criticality is much wider. Since in biological systems, contrary to simulations, it may in general be difficult to reach and mantain a particular state of the system around criticality, it is plausible that the presence of heterogeneity in the self-coupling assemblies could be a clever strategy to guarantee that the system is sufficiently near the criticality to obtained the wanted emergence of a reservoir of timescales.

Chapter 5

Timescales Heterogeneity in Experimental Neural Data

In this chapter, we study the distribution of timescales in experimental data of neural circuits. In the literature, many examples of heterogeneous experimental distributions can be found [32, 66]. In Ref. [32], the single neuron activity of the macaque prefrontal cortex (PFC) regions (dorsolateral prefrontal cortex DLPFC, orbitofrontal cortex OFC, and anterior cingulate cortex ACC) is studied. The data consists of the collection of different trials of single-neuron activity (spike measures). Each trial has a duration of 1s starting from the onset of a fixation period. For each neuron and for each trial, the spikes are histogrammed in 20 bins of 50ms each, giving an estimation of the rate of the single neuron in each trial. The across-trial correlation of the rates is then computed for each neuron using Pearson's correlation coefficient. From the autocorrelation, an exponential decay has been fitted, giving an estimate of the autocorrelation time of the single neuron as the decay time of the exponential. The set of autocorrelation times (1 for each neuron) is then histogrammed and shows a long-tailed distribution that spans several orders of magnitude, from 10ms to 1000ms [32]. In this thesis, we perform a similar analysis on a different neural dataset. Our dataset consists of measures with Ca2+ imaging by means of two-photon microscopy of the mouse olfactory bulb while stimulating.

5.1   Calcium Imaging

Two photons calcium imaging is a very common technique to study the activity of cells in neural circuits [67]. It is a microscopy technique that allows optical measurements of the calcium status (Ca2 +) of an isolated neural cell. The basic idea is to introduce calcium indicators, that is, fluorescent molecules that respond to the binding of Ca2+, encoding them genetically (GECI). When in neurons the action potential is generated, a rapid influx of Ca2+ ions follows, triggering the activation of calcium indicators. With this technique, calcium imaging can be used to monitor electrical activity in hundreds of neurons in neural circuits. In Fig. 5.1 at the top, an example of a calcium imaging trace of a mouse olfactory bulb cell is shown. The trace is expressed in Z-score units, that consists in a normalization of the signal x according to

$$Z = \frac{x - \mu}{\sigma}, \tag{5.1}$$

where μ is the mean of the signal x and σ is the standard deviation. In this data set, mouses are stimulated 10 times (7 times with aromatic oils and 3 times with odorless placebo) every one and a half minutes. At the bottom of Fig. 5.1 the same trace is plotted, overlapped with the reconstructed signal of the trace. For each sampling campaign, different fields have been measured, each of them containing a number of cells varying from 60 to 100. In this analysis, 8 different fields are considered for a total of 568 traces (before the SNR filter described in the following section).
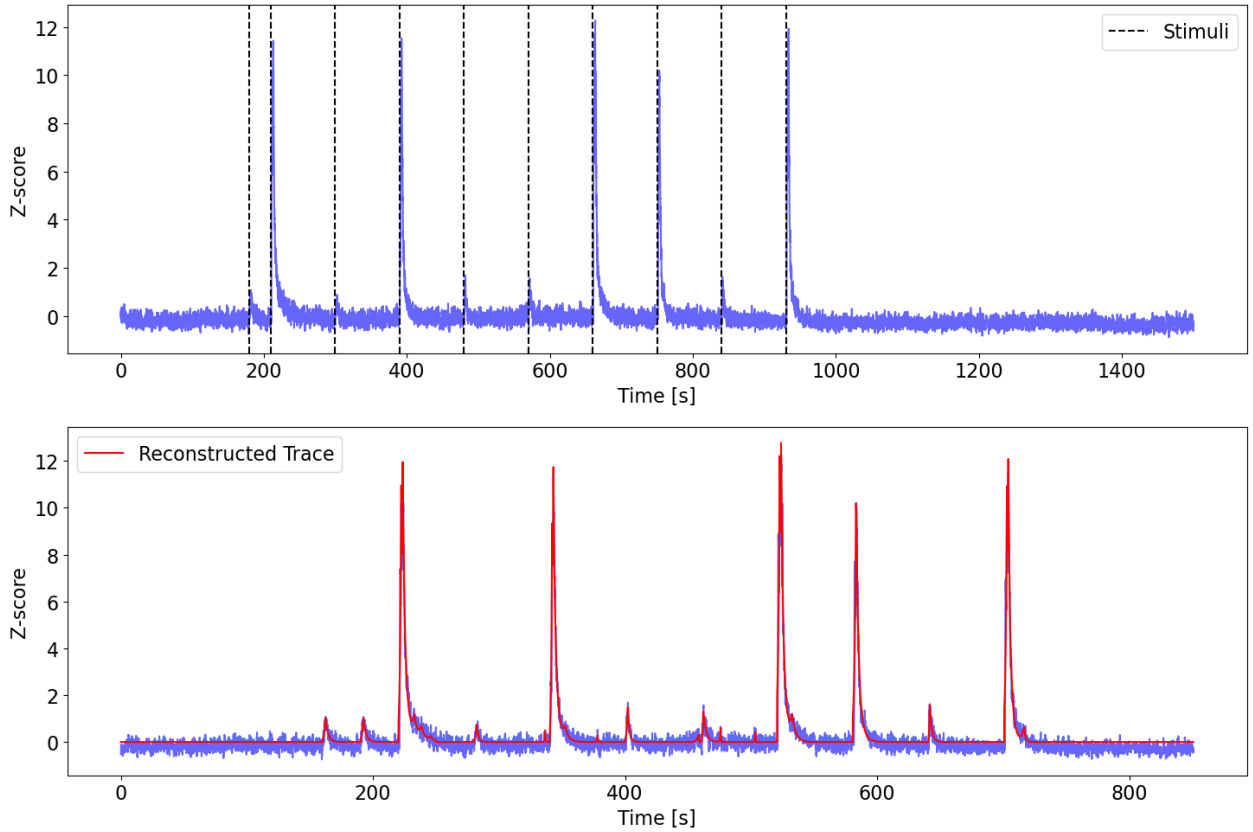
Figure 5.1: Example of Z-score obtain with Calcium-Imaging technique of the cell from the olfactory bulb of a mouse when subject to stimulus. Top: the raw trace with the corresponding stimuli. Bottom: reconstruction of the activity from the raw trace.

5.2 Signal to Noise Ratio

For each trace in each field, a measure of the Signal-to-Noise Ratio (SNR) is obtained as

$$SNR = \frac{Z_{max}}{\sigma_Z}, \tag{5.2}$$

where Z_{max} is the maximum value of the Z-score trace and σ_Z is the standard deviation of a chosen baseline period, as for example, the period at the beginning of the campaign where no stimuli are given. The traces can be ordered by this measure of SNR in each field, and an arbitrary threshold can be chosen to select the traces with higher SNR. In Fig. 5.2, an example of traces of a field ordered by SNR is shown. In the following analysis, we have decided to keep the top 60% of traces by SNR for each field, for a total of 341 traces.

5.3 Denoising of traces

A general model for the noise of Calcium Imaging with complete scientific consensus is not yet available in the literature. The problematic points for such a model are not limited to measurement noise and electrical noise but extend to the behavior of a single cell, which is variable. It is also expected that the noise is not constant along time, but it may depend on the real neural-activity of the cell. A common approach is to use a convolution kernel to smooth the Z-score traces and, therefore, eliminate high-frequency oscillations. In this thesis, we used a Gaussian kernel with a standard deviation of 200 ms. In Fig. 5.3 an example of smoothed trace is presented. All the analysis and the results presented in this thesis are obtained on the traces smoothed with the above-mentioned filter.
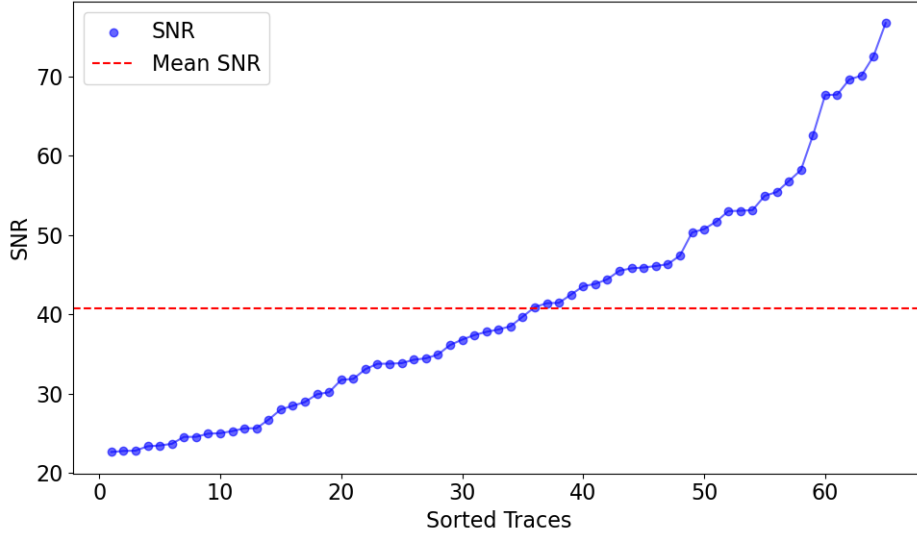
Figure 5.2: Traces of a Field sorted by increasing value of Signal-to-Noise ratio and mean value of the samples of SNR.
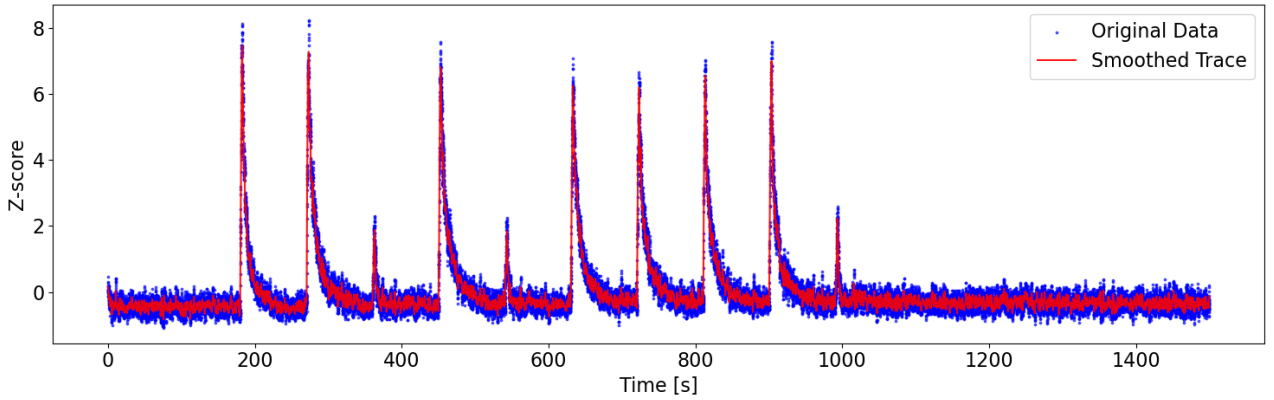

Figure 5.3: Example of smoothed Z-score trace obtained by convolution of the raw trace with a Gaussian kernel with standard deviation of 200 ms.

5.4   Exponential decay Fit of Calcium Events

The Calcium events that follow stimuli, shown in Fig. 5.1, can be fitted with exponential decay. In particular, the traces are divided into time fragments that start when a stimulus is given and last 80 s. The first peak of the traces in every fragment is the point from which the exponential decay is fitted. The time that passes from the stimulus to the peak is listed as the *ascendent* time t_{asc}. We note also that the traces often show a second peak that decays exponentially. In principle, the number of exponential peaks is variable and should be kept as a free parameter of the fit, but here we limit ourselves to two exponential peaks. The function that is fitted is the following:

$$f(t) = A_1 \exp\left(-B_1|t - t_{asc}|\right) + A_2 \exp\left(-B_2|t - t_{asc} - t_{lag}|\right) + C \qquad \text{for } t \geq t_{asc}, \qquad (5.3)$$

where C is an offset and t_{lag} is a free parameter that determines the distance between the exponential peaks. Some examples of fits can be found in Fig. 5.4. From the procedure described above, for each stimulus of each trace we obtain different characteristic times: the *ascendent* time t_{asc}, the half-decay time of the first exponential τ_1, the half-decay time of the second exponential τ_2, and the time-lag between the two calcium events t_{lag}. Collecting their values for all the samples, we can study their statistical distribution, as shown in Fig. 5.5.
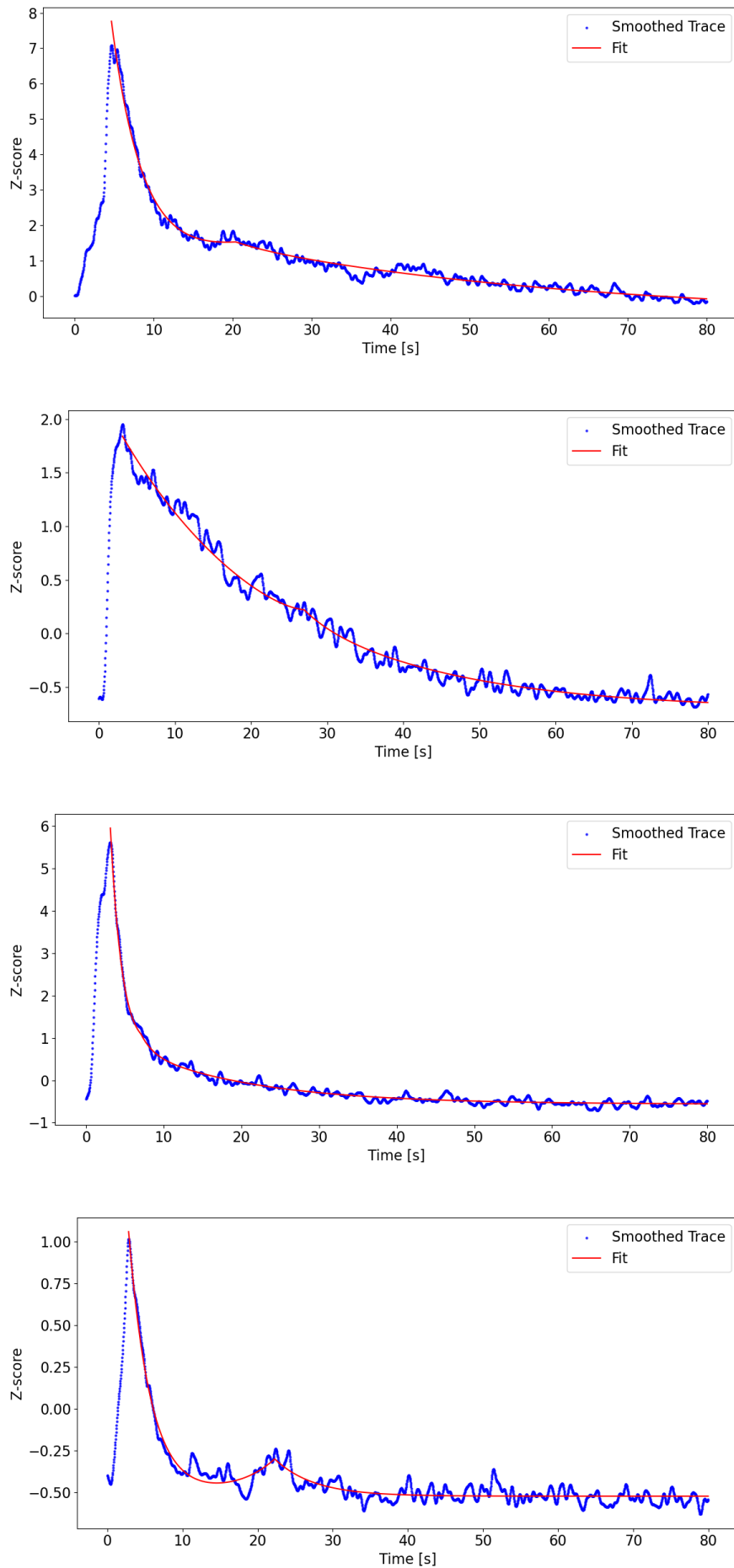
Figure 5.4: Examples of double exponential fit of the calcium events that follow a stimulus at $t = 0$ in a window of 80 s.
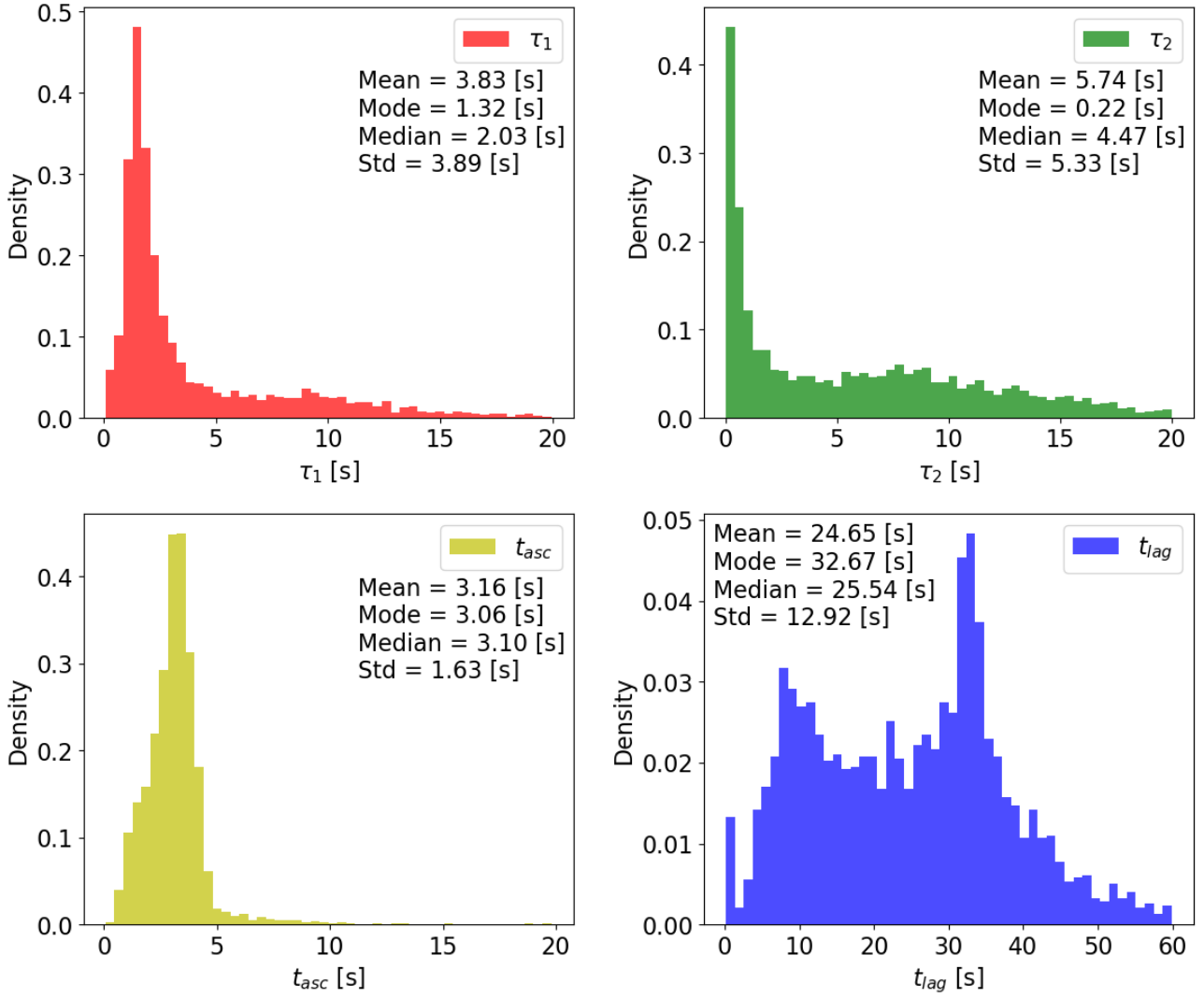
Figure 5.5: Experimental density distributions of the characteristic times τ_1, τ_2, t_{asc}, t_{lag} of calcium events that follow a stimulus

The decay times of the principal and secondary exponential peaks display very heterogeneous distributions, with the difference that the mode of τ_1 is 1.32 s while the mode of τ_2 is much smaller, of 0.22 s, suggesting that most of the second peaks decay very fast. As expected, the ascending time t_{asc} displays a more symmetric distribution with a mean of 3.16 s. This time takes into account the diffusion time of the aromatic oil when injected, the reaction time to the stimulus of the mouse, and the kinetics of the calcium events. The last characteristic time considered is the lag between the two exponential peaks t_{lag} that displays a very particular bi-modal distribution that span across a large window of 60 s. The distribution of these times is of fundamental relevance in the interpretation of the results of following analysis.

5.5 Autocorrelation Function and Power Spectrum

In this section the autocorrelation function $C(\Delta t)$ of the traces is computed, as defined in Eq. (4.12) with the notation introduced in Ref. [31]. In Fig. 5.6 is presented the average over all traces of the autocorrelation function. The autocorrelation function C presents 10 principal bumps that correspond to the calcium events that follow the stimuli injections and 10 secondary bumps that correspond to the second calcium event that is registered after a stimulus. In Fig. 5.7 we plot the average autocorrelation function computed in rest periods (periods of spontaneous activity without stimuli) and after a stimulus. As expected, the correlation is higher in the case of stimulus since the trace typically shows a principal and a secondary calcium events, while during spontaneous activity it is
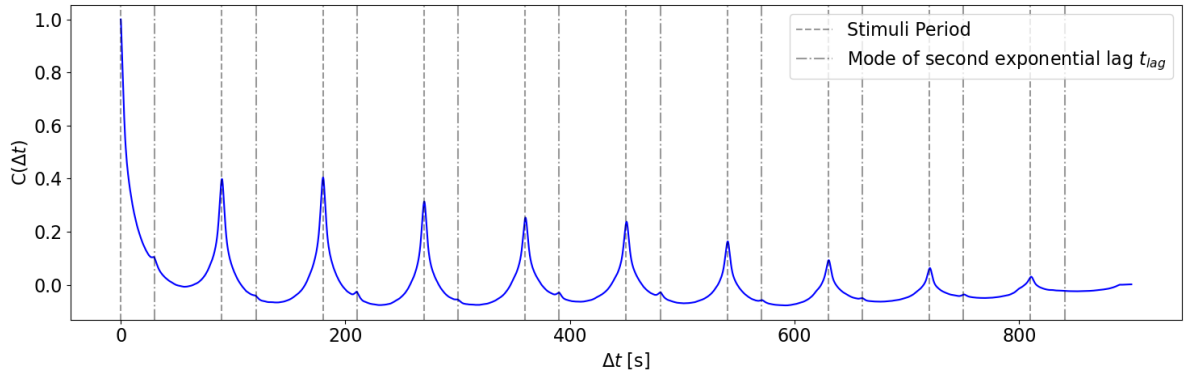
Figure 5.6: Average over all traces of their Autocorrelation function $C(\Delta t)$ and comparison with the period on injection of the stimuli and the expectation time interval between the two calcium events described by the parameter t_{lag}.
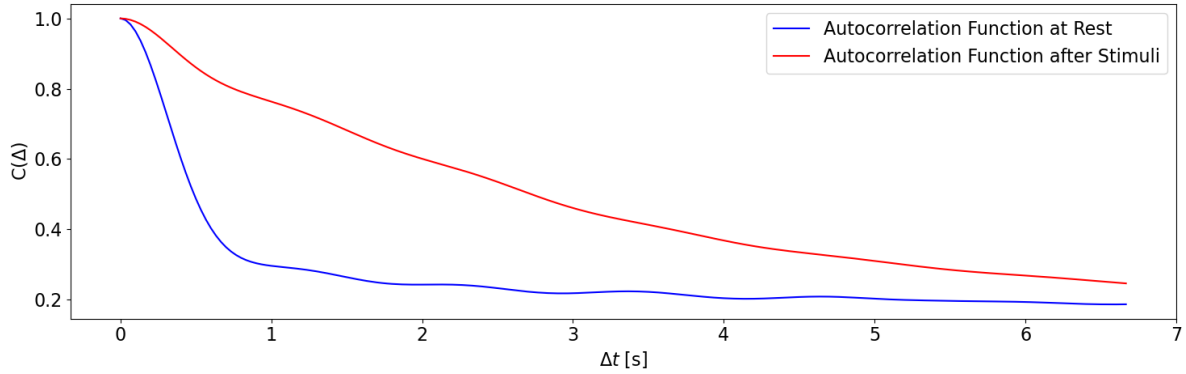

Figure 5.7: Comparison between the average autocorrelation function at rest and after a stimulus.

not guaranteed to observe calcium events. We also compute the power spectrum, as the finite Fourier transform of the autocorrelation function as done in Ref. [68]. In Fig. 5.8, the power spectrum averaged over the traces smoothed with the Gaussian filter is shown. As expected, the peaks in the power spectrum are found at the frequencies of the stimuli and their multiples.
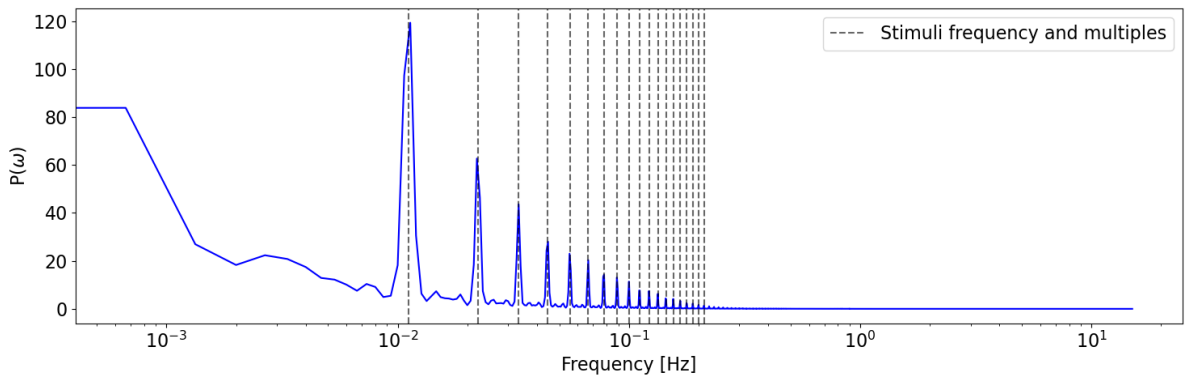

Figure 5.8: Average power spectrum of smoothed traces and comparison with stimuli frequency. Note that the step along the frequencies is limited by the sampling frequency of the measurements $f_{sam} = 30$ Hz.

5.6 Autocorrelation times

The autocorrelation functions shown in the previous section do not always follow an exponential decay behavior. For this reason, we use the Half-Width at Half-Maximum (HWHM) estimator to compute a characteristic autocorrelation time τ. Some examples of HWHM estimations are shown in Fig. 5.9 for

autocorrelation functions computed after a stimulus. Collecting the estimated autocorrelation times
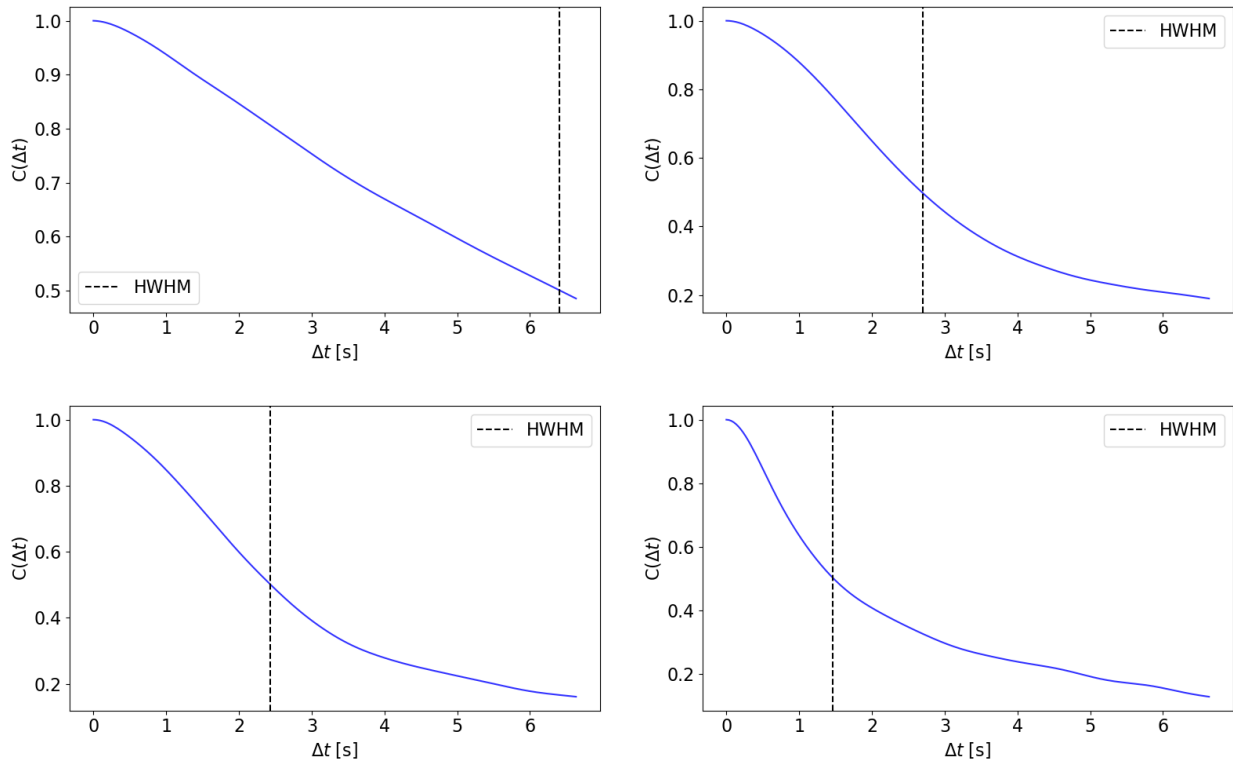

Figure 5.9: Examples of autocorrelation functions after a stimulus and corresponding estimation of the autocorrelation time τ as Half-Width at Half-Maximum of the autocorrelation function $C(\Delta t)$.

for each trace and each stimulus, we can study the statistics of their distribution at rest in Fig. 5.10 and after the stimuli in Fig. 5.11. The distribution of autocorrelation times during the period of spontaneous activity (Fig. 5.10) shows a skewed distribution with a fat tail ranging from 200 to 1200 ms, similarly to the results available in the literature for different neural data sets [32, 66].
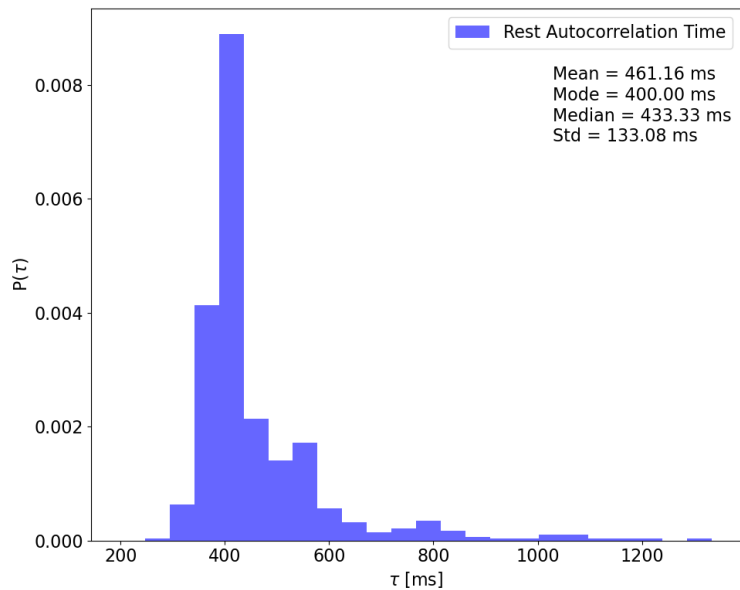

Figure 5.10: Histogram of the autocorrelation times τ obtained from the rest periods of the traces.
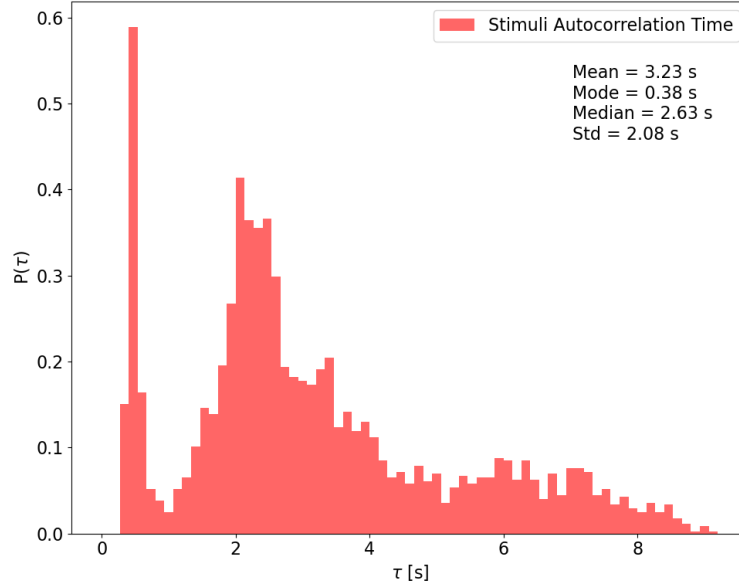
Figure 5.11: Histogram of autocorrelation times τ obtained after the stimuli.

The distribution of autocorrelation times after the stimuli presents two peaks and a thick tail (Fig. 5.11). This peculiar distribution can be interpreted in terms of the characteristic times studied in Fig. 5.5 and the autocorrelation times at rest studied in Fig. 5.10, suggesting that a model for the distribution could be developed. We present here some insights and leave the formalization of such a model for future works. The first bump $P_{fp}(\tau_{rest})$ represents the distribution of the autocorrelation times at rest, the second bump $P_{sp}(t_{asc}, \tau_1)$ is given by the distribution of ascendent times added to the decay times of the principal calcium events, and the tails $P_{tail}(t_{lag}, \tau_2)$ are due to the lag between calcium events added to the decay times of the secondary calcium events. Note that since t_{asc} and t_{lag} are estimated as distances in time, they have been multiplied by a factor $(1 - \log(2))$, assuming exponential behaviors, in order to compare them with times estimated as HWHM. In Fig. 5.12 the distribution of autocorrelation times after stimulus are compared P_{fp}, P_{sp} and P_{tail}, that are not normalized singularly but together, with amplitude chosen arbitrarily to maximize the overlap with the experimental distribution.
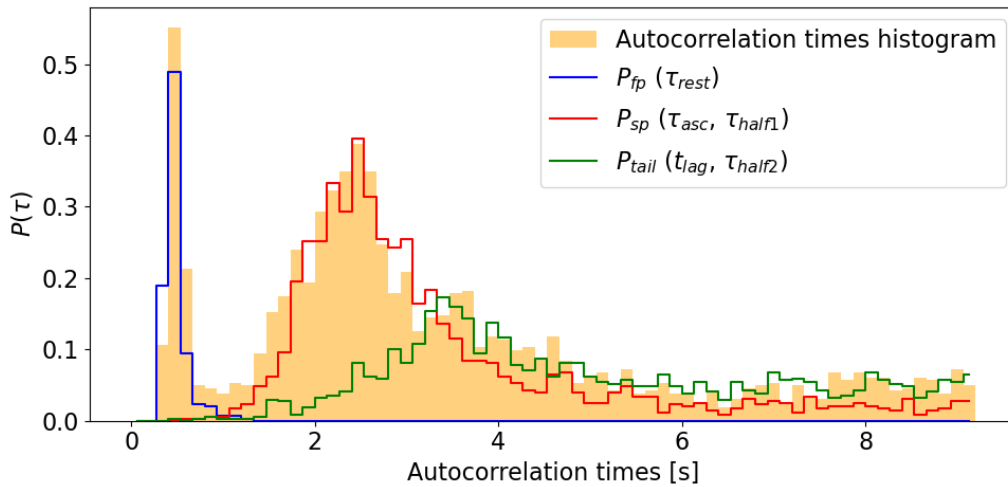

Figure 5.12: Distribution of autocorrelation times after a stimulus and comparison with the characteristic times of the corresponding calcium events and rest baseline. Note that the distributions P_{fp}, P_{sp}, P_{tail} are not normalized in this plot to compare them, individually in each range, with the normalized distribution of autocorrelation times.

Chapter 6

Conclusion

In the field of life sciences, the quantitative description of living systems is known to be tremendously fascinating and complicated. In ecology and neuroscience, for example, systems made up of large numbers of units interacting in nontrivial ways give rise to the emergence of macroscopic patterns, typical of complex systems. Unraveling the intricacy of such systems requires the development of fundamental minimal models that are able to capture the essential features and behavior of the system and that, at the same time, can be treated analytically. In the field of statistical mechanics of complex systems, a large variety of analytical and computational methods has been developed borrowing and adapting results from the fields of stochastic processes, dynamical systems, non-equilibrium statistical physics and many more.

The common thread of the thesis is thus how the Dynamical Mean Field Theory allows analytical insights in complex systems. In particular, the applications of Dynamical Mean Field Theory (DMFT) in ecology and neuroscience have been explored. Contrary to the classical mean-field theories that are applied at stationarity, DMFT captures the dynamical behavior of a system in the thermodynamic limit of a large number of units. Its derivation, as shown in Chapter 2, is based on the theory of generating functional and path integrals and its application is particularly suitable for systems characterized by quenched disorder.

In ecology, the archetype of all models is the Generalized Lotka-Volterra (GLV). The application of DMFT to this model led to interesting results regarding the stability of the system, the Species Abundance Distribution (SAD), and the prediction of the probability of extinction of a species. The DMFT of GLV can also be generalized to modified versions of the model, as done in this thesis. The introduction of a function that saturates species interactions removed the unfeasible unbounded growth phase observed in the standard Generalized Lotka-Volterra model. The DMFT facilitated the derivation of the Species Abundance Distribution of the model. Moreover, performing the Linear Stability Analysis of the DMFT allowed for the identification of the critical line marking the transition from stability to chaos. Both results were validated with numerical simulations of the ordinary differential equations of the GLV. As expected, increasing the saturation parameter K enhanced the stability of the system, while in the limit $K \to 0$ (no saturation) the results known in the literature were recovered. The divergence of the critical line for $\gamma = 0$ indicates that completely anti-symmetric systems, such as those with only predator-prey interactions, are always stable. The simulations used for the validation of the results revealed an interesting peculiarity, highlighted qualitatively in this thesis. In the chaotic phase, two different behaviors of the system were observed, depending on the value of the correlation parameter γ. For large values of γ, that is, mostly symmetric systems, the chaotic phase is characterized by multiple fixed-points that are marginally stable. For lower values of γ, the system's behavior is completely chaotic and volatile. These observations are a consequence of the introduction of the saturation function and may be independent of its functional form. A complete study of this phenomenon in the chaotic phase is left for future works.

In neuroscience, neural circuits are often modeled with Recurrent Neural Networks (RNN). In this

thesis, networks of recurrently connected neural assemblies were analyzed to study the distribution of characteristic timescales, which play a fundamental role in the computation of complex tasks in neural circuits. The dynamic variable in this models is a sort of global spiking rate of the units, standardized to keep values between -1 and 1. The neural assemblies of this model represents the functional ensembles that are experimentally observed in many circuits. Their sizes are typically heterogeneously distributed and are modeled to be proportional to the self-couplings of the units in the rate network. By applying Dynamical Mean Field Theory, the dynamical behavior of the system was predicted for particular distributions $P(s)$ of the self-couplings of the network for different choices of the gain network g, like in the case of constant values of s. The case of a lognormal distribution of $P(s)$ was also explored numerically, and the distribution of autocorrelation times was computed from the simulations. Our analysis suggests that near criticality the system naturally generates a reservoir of timescales. For a fixed distribution of self-couplings, the choice of the gain network determines the system's phase. In the case of constant s, the window around the critical value of g in which the reservoir of timescales is observed is very narrow, while in the case of lognormal $P(s)$ the window is much wider. These insights lead to the plausible hypothesis that biological neural systems may evolve to constitute heterogeneous functional ensembles as a strategy to widen the operating window in which criticality generates a reservoir of timescales, consistent with experimental observations.

In Chapter 5 the empirical distributions of characteristic times in neural systems were studied. The dataset consisted of Calcium Imaging with two-photon microscopy traces from the olfactory bulb of mice. The analysis highlighted that the timescales of the calcium events that follow a stimulus govern the autocorrelation and power spectrum of the calcium traces. In the rest periods (periods of spontaneous activity), the distribution of autocorrelation times was skewed and with fat-tails, akin to other results known in the literature. In the periods of stimulus, a peculiar distribution of autocorrelation times was observed, with two peaks and a fat-tail. Our analysis qualitatively shows that these patterns can be explained in terms of the rest autocorrelation times distributions and the characteristic timescales of the calcium events following a stimulus. The development of a quantitative model is left as a possible future work.

Overall, this master thesis provides a review of the Dynamical Mean Field Theory, which is an exceptional tool to unravel the intricacy of complex systems. Its application in the field of ecology and neuroscience offers new perspectives on the dynamics of these peculiar systems and aids in the interpretation of emergent patterns similar to those observed in experimental data.

Bibliography

[1] Philip W Anderson. "More Is Different: Broken symmetry and the nature of the hierarchical structure of science." In: *Science* 177.4047 (1972), pp. 393–396.

[2] Nigel Goldenfeld and Leo P Kadanoff. "Simple lessons from complexity". In: *science* 284.5411 (1999), pp. 87–89.

[3] Mark EJ Newman. "Complex systems: A survey". In: *arXiv preprint arXiv:1112.1440* (2011).

[4] Scott Camazine et al. "Self-organization in biological systems". In: *Self-Organization in Biological Systems*. Princeton university press, 2020.

[5] S Swain. "Handbook of stochastic methods for physics, chemistry and the natural sciences". In: *Optica Acta: International Journal of Optics* 31.9 (1984), pp. 977–978.

[6] Paul C Bressloff. *Stochastic processes in cell biology*. Vol. 41. Springer, 2014.

[7] Kerson Huang. *Statistical mechanics*. John Wiley & Sons, 2008.

[8] James P Sethna. *Statistical mechanics: entropy, order parameters, and complexity*. Vol. 14. Oxford University Press, USA, 2021.

[9] Albert-László Barabási. "Network science". In: *Philosophical Transactions of the Royal Society A: Mathematical, Physical and Engineering Sciences* 371.1987 (2013), p. 20120375.

[10] John M Ziman. *Models of disorder: the theoretical physics of homogeneously disordered systems*. Cambridge university press, 1979.

[11] Marc Mézard, Giorgio Parisi, and Miguel Angel Virasoro. *Spin glass theory and beyond: An Introduction to the Replica Method and Its Applications*. Vol. 9. World Scientific Publishing Company, 1987.

[12] Masud Chaichian and Andrei Demichev. *Path integrals in physics: Volume I stochastic processes and quantum mechanics*. CRC Press, 2018.

[13] Tobias Galla. "Generating-functional analysis of random Lotka-Volterra systems: A step-by-step guide". In: *arXiv preprint arXiv:2405.14289* (2024).

[14] Paul Cecil Martin, ED Siggia, and HA Rose. "Statistical dynamics of classical systems". In: *Physical Review A* 8.1 (1973), p. 423.

[15] C. De Dominicis. "Dynamics as a substitute for replicas in systems with quenched random impurities". In: *Phys. Rev. B* 18 (9 Nov. 1978), pp. 4913–4919. DOI: `10.1103/PhysRevB.18.4913`. URL: `https://link.aps.org/doi/10.1103/PhysRevB.18.4913`.

[16] Hans-Karl Janssen. "On a Lagrangean for classical field dynamics and renormalization group calculations of dynamical critical properties". In: *Zeitschrift für Physik B Condensed Matter* 23.4 (1976), pp. 377–380.

[17] Felix Roy et al. "Numerical implementation of dynamical mean field theory for disordered systems: Application to the Lotka–Volterra model of ecosystems". In: *Journal of Physics A: Mathematical and Theoretical* 52.48 (2019), p. 484001.

[18] Anastasios Tsoularis and James Wallace. "Analysis of logistic growth models". In: *Mathematical biosciences* 179.1 (2002), pp. 21–55.

[19] Robert Mac Arthur. "Species packing, and what competition minimizes". In: *Proceedings of the National Academy of Sciences* 64.4 (1969), pp. 1369–1371.

[20] Ofer Malcai et al. "Theoretical analysis and simulations of the generalized Lotka-Volterra model". In: *Physical Review E* 66.3 (2002), p. 031102.

[21] Peter J Wangersky. "Lotka-Volterra population models". In: *Annual Review of Ecology and Systematics* 9 (1978), pp. 189–218.

[22] Valentina Ros et al. "Generalized lotka-volterra equations with random, nonreciprocal interactions: The typical number of equilibria". In: *Physical Review Letters* 130.25 (2023), p. 257401.

[23] Robert M May. *Stability and complexity in model ecosystems*. Princeton university press, 2019.

[24] Tobias Galla. "Dynamically evolved community size and stability of random Lotka-Volterra ecosystems (a)". In: *Europhysics Letters* 123.4 (2018), p. 48004.

[25] Guy Bunin. "Ecological communities with Lotka-Volterra dynamics". In: *Physical Review E* 95.4 (2017), p. 042414.

[26] Laura Sidhom and Tobias Galla. "Ecological communities from random generalized Lotka-Volterra dynamics with nonlinear feedback". In: *Physical Review E* 101.3 (2020), p. 032101.

[27] Lyle Poley, Tobias Galla, and Joseph W Baron. "Interaction networks in persistent Lotka-Volterra communities". In: *arXiv preprint arXiv:2404.08600* (2024).

[28] Omri Barak. "Recurrent neural networks as versatile tools of neuroscience research". In: *Current opinion in neurobiology* 46 (2017), pp. 1–6.

[29] Jascha Achterberg et al. "Spatially embedded recurrent neural networks reveal widespread links between structural and functional neuroscience findings". In: *Nature Machine Intelligence* 5.12 (2023), pp. 1369–1381.

[30] Laura E Suárez et al. "Connectome-based reservoir computing with the conn2res toolbox". In: *Nature Communications* 15.1 (2024), p. 656.

[31] Iris Ginzburg and Haim Sompolinsky. "Theory of correlations in stochastic neural networks". In: *Physical review E* 50.4 (1994), p. 3171.

[32] Sean E Cavanagh et al. "Autocorrelation structure at rest predicts value correlates of single neurons during reward-guided choice". In: *elife* 5 (2016), e18937.

[33] Nicolas Perez-Nieves et al. "Neural heterogeneity promotes robust learning". In: *Nature communications* 12.1 (2021), p. 5791.

[34] Haim Sompolinsky, Andrea Crisanti, and Hans-Jurgen Sommers. "Chaos in random neural networks". In: *Physical review letters* 61.3 (1988), p. 259.

[35] Merav Stern, Haim Sompolinsky, and Laurence F Abbott. "Dynamics of random neural networks with bistable units". In: *Physical Review E* 90.6 (2014), p. 062710.

[36] Merav Stern, Nicolae Istrate, and Luca Mazzucato. "A reservoir of timescales emerges in recurrent circuits with heterogeneous neural assemblies". In: *Elife* 12 (2023), e86552.

[37] Rodrigo Perin, Thomas K Berger, and Henry Markram. "A synaptic organizing principle for cortical neuronal groups". In: *Proceedings of the National Academy of Sciences* 108.13 (2011), pp. 5419–5424.

[38] Moritz Helias and David Dahmen. *Statistical field theory for neural networks*. Vol. 970. Springer, 2020.

[39] Carson C Chow and Michael A Buice. "Path integral methods for stochastic differential equations". In: *The Journal of Mathematical Neuroscience (JMN)* 5 (2015), pp. 1–35.

[40] Luigi M Ricciardi. "On the transformation of diffusion processes into the Wiener process". In: *Journal of Mathematical Analysis and Applications* 54.1 (1976), pp. 185–199.

[41] Hannes Risken and Hannes Risken. *Fokker-planck equation*. Springer, 1996.

[42] Lars Onsager and Stefan Machlup. "Fluctuations and irreversible processes". In: *Physical Review* 91.6 (1953), p. 1505.

[43] Horacio S Wio et al. "Path-integral formulation for stochastic processes driven by colored noise". In: *Physical Review A* 40.12 (1989), p. 7312.

[44] Jannis Schuecker et al. "Functional methods for disordered neural networks". In: *arXiv preprint arXiv:1605.06758* (2016).

[45] Juan C Meza. "Steepest descent". In: *Wiley Interdisciplinary Reviews: Computational Statistics* 2.6 (2010), pp. 719–722.

[46] Marco Zenari. *Dynamical Mean Field Theory and Applications to Ecological and Neural Systems*. https://github.com/MarcoZenari/Dynamical_Mean_Field_Theory_and_Applications_to_Ecological_and_Neural_Systems. 2024.

[47] Vito Volterra. "Variations and fluctuations of the number of individuals in animal species living together". In: *ICES Journal of Marine Science* 3.1 (1928), pp. 3–51.

[48] Alfred J Lotka. "Analytical note on certain rhythmic relations in organic systems". In: *Proceedings of the National Academy of Sciences* 6.7 (1920), pp. 410–415.

[49] Ada Altieri et al. "Properties of equilibria and glassy phases of the random lotka-volterra model with demographic noise". In: *Physical Review Letters* 126.25 (2021), p. 258301.

[50] AR Batista-Tomás, Andrea De Martino, and Roberto Mulet. "Path-integral solution of MacArthur's resource-competition model for large ecosystems with random species-resources couplings". In: *Chaos: An Interdisciplinary Journal of Nonlinear Science* 31.10 (2021).

[51] Peter Dayan and Laurence F Abbott. *Theoretical neuroscience: computational and mathematical modeling of neural systems*. MIT press, 2005.

[52] Idan Segev. "Single neurone models: oversimple, complex and reduced". In: *Trends in neurosciences* 15.11 (1992), pp. 414–421.

[53] Larry J Millet and Martha U Gillette. "Over a century of neuron culture: from the hanging drop to microfluidic devices". In: *The Yale journal of biology and medicine* 85.4 (2012), p. 501.

[54] David Sussillo. "Neural circuits as computational dynamical systems". In: *Current opinion in neurobiology* 25 (2014), pp. 156–163.

[55] Anagh Pathak, Dipanjan Roy, and Arpan Banerjee. "Whole-brain network models: from physics to bedside". In: *Frontiers in Computational Neuroscience* 16 (2022), p. 866517.

[56] Janice Chen, Uri Hasson, and Christopher J Honey. "Processing timescales as an organizing principle for primate cortex". In: *Neuron* 88.2 (2015), pp. 244–246.

[57] Kiyohito Iigaya et al. "Deviation from the matching law reflects an optimal strategy involving learning over multiple timescales". In: *Nature communications* 10.1 (2019), p. 1466.

[58] György Buzsáki and James J Chrobak. "Temporal structure in spatially organized neuronal ensembles: a role for interneuronal networks". In: *Current opinion in neurobiology* 5.4 (1995), pp. 504–510.

[59] James H Marshel et al. "Cortical layer–specific critical dynamics triggering perception". In: *Science* 365.6453 (2019), eaaw5202.

[60] Nicolas Brunel. "Dynamics of sparsely connected networks of excitatory and inhibitory spiking neurons". In: *Journal of computational neuroscience* 8 (2000), pp. 183–208.

[61] David Wyrick and Luca Mazzucato. "State-dependent regulation of cortical processing speed via gain modulation". In: *Journal of Neuroscience* 41.18 (2021), pp. 3988–4005.

[62] Donald O Hebb. "Organization of behavior. new york: Wiley". In: *J. Clin. Psychol* 6.3 (1949), pp. 335–307.

[63] Larry F Abbott. "Lapicque's introduction of the integrate-and-fire model neuron (1907)". In: *Brain research bulletin* 50.5-6 (1999), pp. 303–304.

[64] Yashar Ahmadian, Francesco Fumarola, and Kenneth D Miller. "Properties of networks with partially structured and partially random connectivity". In: *Physical Review E* 91.1 (2015), p. 012820.

[65] Madan Lal Mehta. *Random matrices*. Elsevier, 2004.

[66] Alberto Bernacchia et al. "A reservoir of time constants for memory traces in cortical neurons". In: *Nature neuroscience* 14.3 (2011), pp. 366–372.

[67] Christine Grienberger and Arthur Konnerth. "Imaging calcium in neurons". In: *Neuron* 73.5 (2012), pp. 862–885.

[68] Kanaka Rajan, LF Abbott, and Haim Sompolinsky. "Stimulus-dependent suppression of chaos in recurrent neural networks". In: *Physical review e* 82.1 (2010), p. 011903.